BNL-224979-2023-TECH

EIC-ADD-TN-077

Resonance Island Jump theory for the HSR

S. Peggs

October 2023

Electron-Ion Collider Project

Brookhaven National Laboratory

U.S. Department of Energy

USDOE Office of Science (SC), Nuclear Physics (NP) (SC-26)

Notice: This technical note has been authored by employees of Brookhaven Science Associates, LLC under Contract No.DE-SC0012704 with the U.S. Department of Energy. The publisher by accepting the technical note for publication acknowledges that the United States Government retains a non-exclusive, paid-up, irrevocable, world-wide license to publish or reproduce the published form of this technical note, or allow others to do so, for United States Government purposes.

DISCLAIMER

This report was prepared as an account of work sponsored by an agency of the United States Government. Neither the United States Government nor any agency thereof, nor any of their employees, nor any of their contractors, subcontractors, or their employees, makes any warranty, express or implied, or assumes any legal liability or responsibility for the accuracy, completeness, or any third party's use or the results of such use of any information, apparatus, product, or process disclosed, or represents that its use would not infringe privately owned rights. Reference herein to any specific commercial product, process, or service by trade name, trademark, manufacturer, or otherwise, does not necessarily constitute or imply its endorsement, recommendation, or favoring by the United States Government or any agency thereof or its contractors or subcontractors. The views and opinions of authors expressed herein do not necessarily state or reflect those of the United States Government or any agency thereof.

Resonance Island Jump theory for the HSR

S. Peggs, H. Lovelace III, G. Robert-Demolaize, T. Satogata.

October 31, 2023

Abstract

The Resonance Island Jump (RIJ) scheme for transition crossing in HSR (or the CERN SPS [1, 2]) is radically new, and untested. Beam experiments in RHIC will be necessary if the RIJ scheme is to be considered as a serious alternative to upgrading the first order linear jump scheme currently implemented in RHIC [3]. This note outlines the planning and the theoretical foundations that are necessary for such a beam experiment, perhaps to be performed in 2024.

Contents

1 The potential for RIJ-related beam experiments in RHIC **3**
- 1.1 Key parameters of interest . . . 3
- 1.2 Adiabatically opening or closing resonance islands . . . 3
- 1.3 Modulating the RHIC tune with transition jump quadrupoles . . . 4

2 Octupoles and detuning in RHIC and HSR **6**
- 2.1 The horizontal detuning coefficient κ . . . 7
- 2.2 Detuning coefficient ranges in both planes . . . 9

3 Motion close to the 1/4 resonance **11**
- 3.1 One-turn motion . . . 11
- 3.2 Four-turn motion . . . 11
- 3.3 Four-turn detuning . . . 13
- 3.4 The action of the fixed point at the center of a resonance island . . . 14
- 3.5 Standard map motion around the island center . . . 14
- 3.6 Resonance island width . . . 15
- 3.7 Resonance island tunes . . . 16

4 Evaluating the resonance driving vector $\bar{V}_{44}$ **18**
- 4.1 One octupole, one turn . . . 18
- 4.2 Many octupoles, four turns . . . 19
- 4.3 Resonance driving sensitivity vectors $\vec{S}_{PS}$ . . . 20

5 Ramping and modulating the tune **22**
- 5.1 Slow linear tune ramps . . . 22
- 5.2 Slow sinusoidal tune modulation . . . 23
- 5.3 Rapid sinusoidal tune modulation . . . 23
- 5.4 Synchrobetatron sidebands and islands . . . 24

5.5 Synchrobetatron sideband overlap . . . 25
5.6 Dynamical partitions in tune modulation parameter space . . . 25

6 Tune modulation and data reduction techniques **27**
6.1 Data analysis and a summary of E778 results . . . 28
6.2 Fine structure in the partition boundaries . . . 30

7 Summary **32**

Appendices **33**

A Key equations **33**

B Phase spaces, action-angle co-ordinates, emittance, and beam size **34**

C Fixed point finder **36**

List of Figures

1 Transition jumps with both signs of $\gamma_T - \gamma_{TI}$. . . . 3
2 A lattice with one octupole. . . . 6
3 Octupoles and their power supplies in RHIC. . . . 8
4 The separatrix contours of a 4-island chain. . . . 15
5 Change of action due to one octupole of strength g. . . . 18
6 Island sensitivity vectors $\vec{S}_{PS}$. . . . 21
7 Dynamical partitions in (q, Q_M) space for an $N = 4$ resonance. . . . 26
8 Simulated phase space of the Tevatron in the E778 experiment. . . . 27
9 Raw persistent signal loss due to a tune modulation chirp. . . . 28
10 Fourier persistent signal loss due to a tune modulation chirp. . . . 28
11 Measuring the island tune Q_I by locating a boundary in (q, Q_M) space. . . . 29
12 Locating the boundaries in (q, Q_M) space by simulation. . . . 29
13 Representative phase space portraits in different parts of (q, Q_M) space. . . . 31
14 The physical phase space ellipse with action J . . . 35

List of Tables

1 Jump quad power supply tune modulation sensitivities. . . . 5
2 RHIC arc corrector parameters. . . . 7
3 RHIC and HSR detuning coefficient ranges. . . . 10
4 Octupole power supply island sensitivities $\vec{S}_{PS}$. . . . 20
5 Island sensitivities $\vec{S}_{PS}$ for the three effective octupole power supplies . . . 21

1 The potential for RIJ-related beam experiments in RHIC

1.1 Key parameters of interest

Stored beam is usually found on a closed orbit that repeats itself every turn, near the design trajectory at the center of the beam pipe. A horizontal phase space portrait of the motion (including its nonlinear distortions) is taken by developing a Poincaré surface of section, for example plotting (x, x') turn-by-turn for a set of interesting initial conditions. Small amplitude horizontal motion around that closed orbit is then characterized by the closed orbit displacement and angle at a reference point, by Twiss parameters, tune, chromaticity, and the transition gamma: $x_{CO}, x'_{CO}, \beta_x, \alpha_x, Q_x, \chi_x$, and γ_T.

In an RIJ scheme, beam is trapped in a resonance island just before or after transition, so that horizontal closed orbit motion repeats itself, exactly, every N turns. This note assumes that $N = 4$, with many octupoles driving the resonance to first order in their strengths. In this case a Poincaré surface of section that is taken every N turns shows how a set of individual particles that is trapped in a resonance island circulates around an island center. All such trapped particles have a betatron tune of exactly $Q_x = 1/4$ (or $3/4$), even if they have a non-zero momentum offset, $\delta = \Delta p/p$. Each of the N islands is characterized by its own local values – closed orbit and Twiss parameters – that apply at the reference point: x_I, x'_I, β_I, and α_I. All of the islands have the same global parameters – island tune, island chromaticity, and island transition gamma: Q_I, χ_I, and γ_{TI}.

A successful RIJ scheme will have very different on-axis and island transition gammas,

$$|\gamma_T - \gamma_{TI}| \gg 1 \tag{1}$$

where the sign of the difference determines whether beam is kicked into or out of one or N resonance islands at transition time, as illustrated in Figure 1. It may well be that the island chromaticity, defined by

$$\chi_I \equiv \frac{dQ_I}{d\delta} \tag{2}$$

must be acceptably small for an RIJ scheme to be successful, since a strong variation of Q_I with δ may severely limit the momentum range of particles that can be trapped. In all cases the on-momentum island tune Q_I is a parameter of crucial importance.

The three global parameters – Q_I, χ_I, and γ_{TI} – are of vital interest to beam experiments and simulation studies. Do theoretical predictions, simulations, and beam experiments agree on their values? Only if they agree can we confidently design a reliable RIJ scheme.

1.2 Adiabatically opening or closing resonance islands

A fast kicker must be used to move the beam between locations in phase space with sufficiently different values of γ_T, as the beam accelerates through transition. Figure 1 illustrates how beam must either arrive at transition already trapped in one or N islands, or must depart transition trapped in one island, depending on the sign of $\gamma_T - \gamma_{TI}$. The desire to avoid the cost, complexity, and inefficiencies of performing *two* fast

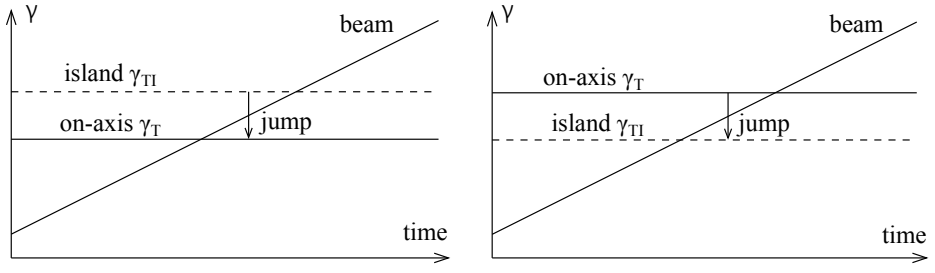


Figure 1: A single jump made with a fast kicker, as the beam γ accelerates through transition.
Left, $\gamma_{TI} > \gamma_T$: beam that was previously captured in one or N islands is kicked on-axis.
Right, $\gamma_{TI} < \gamma_T$: beam that was on-axis is kicked into a single island, in one turn.

kicker jumps – one before and one after transition – can be met by adiabatically opening or closing the islands, well before or long after transition.

Opening the islands adiabatically before transition crossing populates each one identically. This makes it necessary to kick the beam back on-axis over N turns. In a very similar fashion the CERN-PS routinely populates 4 islands in the Multiturn Resonance Extraction scheme, before kicking the beam into an extraction channel [4, 5, 6, 7, 8, 9]. In contrast, the fast kicker can move all the beam into one island in a single turn before transition, with later adiabatic closure, if $\gamma_{TI} < \gamma_T$.

Such a fast kicker, whether one-turn or N-turn, is not available for RHIC beam studies. Nonetheless, RHIC beam studies could adiabatically open and close islands for measurements and observations, for example during repeated beam stores at injection energy. This would enable Q_I and potentially χ_I to be measured using externally applied tune modulation chirps, using techniques similar to those employed in the E778 nonlinear beam dynamics experiment at the Tevatron. This is discussed further in Section 6, along with the E778 data reduction techniques that also have potential for use in RHIC beam studies.

Beam that has been adiabatically trapped in N resonance islands could be accelerated through transition in RHIC, enabling γ_{TI} to be measured directly. Thus, all three vital global quantities – Q_I, χ_I, and γ_{TI} – may be measured in RHIC beam studies, without a fast kicker and without hardware changes to the current RHIC configuration. Local measurements could also be made, for example using ionization profile monitors and pairs of turn-by-turn capable beam position monitors. Turn-by-turn data could also be used to build "Empirical Hamiltonians" [10].

1.3 Modulating the RHIC tune with transition jump quadrupoles

Section 6 shows how externally applied tune modulation chirps were used to measure Q_I values in the E778 experiment. In a RHIC experiment such tune modulation could be provided (somewhat ironically) by repurposing the transition jump quadrupoles themselves.

The horizontal tune shift due to a family of jump quads is

$$\Delta Q \;=\; K1L.\frac{1}{4\pi}\sum_{\text{quads}}\beta \tag{3}$$

where the jump quad power supply strength

$$K1L \;=\; 1/f \tag{4}$$

is the focal strength of a single quad [3]. A maximum current of ± 50 A delivers ± 1.5 Tm [11], so

$$K1L \;=\; \frac{1.5}{50\,(B\rho)}\,.\,I \tag{5}$$

for current I. For example, if RHIC beam studies are performed at a gold injection energy of approximately 10.0 GeV/u, with a rigidity of $B\rho = 82.8$ Tm, then

$$K1L\ [\mathrm{m}^{-1}] \;=\; 3.62\times 10^{-4}\,.\,I\ [\mathrm{A}] \tag{6}$$

in all the quadrupoles driven in series by a single power supply.

The tune shift due to all the quadrupoles driven by a single power supply is

$$\Delta Q \;=\; 3.62\times 10^{-4}\,.\,S_{TM}\,.\,I\ [\mathrm{A}] \tag{7}$$

where the RHIC Blue ring power supply tune modulation sensitivities

$$S_{TM} \;\equiv\; \frac{1}{4\pi}\sum_{\text{quads}}\beta \tag{8}$$

are evaluated in Table 1, in transition optics with $\beta^* = 10$ m in both planes at every IP [3]. Their values fall in the relatively narrow range

$$14.6\ \mathrm{m} \;<\; S_{TM} \;<\; 17.8\ \mathrm{m} \tag{9}$$

Jump quad power supply name	**Tune modulation sensitivity** S_{TM} [m]
bi1-qgt-ps	17.804
bo2-qgt-ps	14.602
bo3-qgt-ps	14.851
bi4-qgt-ps	14.750
bi5-qgt-ps	17.814
bo6-qgt-ps	14.615
bo7-qgt-ps	14.781
bi8-qgt-ps	14.828
bi9-qgt-ps	17.736
bo10-qgt-ps	14.596
bo11-qgt-ps	14.849
bi12-qgt-ps	14.769

Table 1: Jump quad power supply tune modulation sensitivities in the RHIC Blue ring in the 2023 layout with $\beta^* = 10$ m in both planes at every IP [3].

with an average value of

$$\langle S_{TM} \rangle \approx 16.0 \text{ m} \tag{10}$$

that delivers

$$\Delta Q \approx 0.0058 \, . \, I \text{ [A]} \tag{11}$$

Typical large tune shifts of order 0.01 only require a current amplitude I_{AC} of a couple of amps, where

$$I = I_{DC} + I_{AC} \sin(2\pi f t) \tag{12}$$

and where frequencies as high as $f = 100$ Hz are desirable.

2 Octupoles and detuning in RHIC and HSR

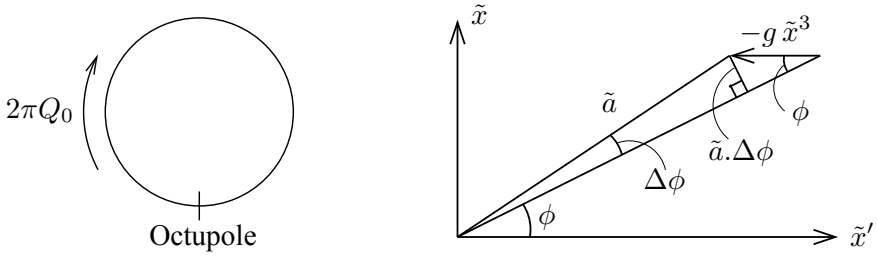


Figure 2: A lattice with one octupole, and the octupole kick in horizontal normalized phase space $(\tilde{x}, \tilde{x}')$.

One-turn motion in a single octupole lattice is sketched in Figure 2, using some of the conventions and definitions for physical, normalized and action-angle phase spaces that are stated in Appendix B. Starting at an observation point just before the octupole, there is first an angular kick that in physical space is

$$\Delta x' \;=\; -g_p x^3 \tag{13}$$

where the integrated octupole strength g_p has the dimension of m^{-3}, if x is measured in meters. In normalized phase space the octupole kick is

$$\Delta \tilde{x}' \;=\; -g\tilde{x}^3 \tag{14}$$

where the normalized integrated strength g has the dimension of m^{-1}, since

$$g \;=\; g_p \beta^2 \tag{15}$$

One-turn motion after the kick is completed by a phase space rotation of

$$\Delta\phi \;=\; 2\pi Q_0 \tag{16}$$

in normalized phase space, where Q_0 is the tune of a particle with a vanishingly small oscillation amplitude.

The RHIC online model and MAD-X use the same convention to quantify the local octupole strength, namely

$$K3\;[\mathrm{m}^{-4}] \;=\; \frac{1}{(B\rho)}\frac{d^3B_y}{dx^3} \tag{17}$$

where the vertical field at displacement x is given by

$$B_y \;=\; \frac{1}{6}\,\frac{d^3B_y}{dx^3}\,x^3 \tag{18}$$

The horizontal angular kick is

$$\Delta x' \;=\; -\frac{B_y L}{(B\rho)} \;=\; -g_p x^3 \tag{19}$$

where $L = 0.583$ m is the effective length of the octupole [11], showing that a thin octupole has physical and normalized strengths

$$\begin{aligned} g_p\;[\mathrm{m}^{-3}] \;&=\; \frac{L}{6}\,\frac{1}{(B\rho)}\,\frac{d^3B_y}{dx^3} \;=\; \frac{1}{6}\,K3.L \\ g\;[\mathrm{m}^{-1}] \;&=\; \frac{\beta^2}{6}\,K3.L \end{aligned} \tag{20}$$

Equations 17 and 18 show that

$$\frac{d^3B_y}{dx^3}\;[\mathrm{Tm}^{-3}] \;=\; \frac{6}{(0.025)^3}\,B_{25}\;[\mathrm{T}] \tag{21}$$

where B_{25} is the vertical field at a displacement of 25 mm. The integrated geometric octupole strength is

$$K3.L\ [\mathrm{m}^{-3}] \ = \ \frac{L}{(B\rho)}\frac{d^3B_y}{dx^3}[\mathrm{m}^{-3}] \tag{22}$$

at a given rigidity, or

$$K3.L\ [\mathrm{m}^{-3}] \ = \ 3.84\times10^5\frac{L}{(B\rho)}B_{25}[\mathrm{T}] \tag{23}$$

Multipole	**Inductance**	**Operating current**	**B-field at 25 mm B_{25}**	**Effective length**	**Quench current**
	mH	A	T	m	A
Decapole	5	59.0	0.016	0.575	202
Octupole	8	50.6	0.017	0.571	198
Quadrupole	29	49.8	0.067	0.555	190
Dipole	840	52.2	0.596	0.508	160

Table 2: RHIC arc corrector parameters [12]. All corrector power supplies are bipolar.

Table 2 lists the operating parameters of the octupoles and other arc correctors, as recorded in the RHIC Configuration Manual [12]. The effective length and B_{25} value listed there yield an integrated strength bipolar range of

$$(K3.L)_{range} \ = \ \pm\frac{3.728\times10^3}{(B\rho)}\ [\mathrm{m}^{-3}] \tag{24}$$

For example, gold rigidities at injection (10 GeV/u) and top storage energy (110 GeV/u) are $(B\rho) = 82.8$ Tm and 914.8 Tm, respectively, with octupole strength ranges of

$$\begin{aligned} (K3.L)_{range} &= \pm45.02\ [\mathrm{m}^{-3}] \qquad \text{injection} \\ &= \pm\ 4.08\ [\mathrm{m}^{-3}] \qquad \text{storage} \end{aligned} \tag{25}$$

Figure 3 shows the layout of the octupoles and their power supplies on either side of a typical RHIC Insertion Region (IR).

2.1 The horizontal detuning coefficient κ

The kick sketched in normalized phase space in Figure 2 causes an additional phase advance of

$$\begin{aligned} \Delta\phi &= g\tilde{a}^2\ \sin^4(\phi) \\ &= g\tilde{a}^2\ \left(\frac{3}{8}-\frac{1}{2}\cos(2\phi)+\frac{1}{8}\cos(4\phi)\right) \end{aligned} \tag{26}$$

The normalized amplitude $\tilde{a}$ is often constant to a good approximation for near-linear non-resonant motion, in which case the amplitude and phase on turn n are

$$\begin{aligned} \tilde{a}_n &\approx \tilde{a} = \text{constant} \\ \phi_n &\approx 2\pi Q_0.n + \phi_0 \end{aligned} \tag{27}$$

Since the phase ϕ_n advances smoothly turn-by-turn, the trigonometric averages

$$\begin{aligned} \langle\cos(2\phi)\rangle &\approx 0 \\ \langle\cos(4\phi)\rangle &\approx 0 \end{aligned} \tag{28}$$

apply as $n\to\infty$ if Q_0 is not a rational fraction. Combining Equations 26 and 28 shows that the average additional phase advance per turn is

$$\langle\Delta\phi\rangle \ = \ g\tilde{a}^2\ \left\langle\sin^4(\phi)\right\rangle \ = \ \frac{3}{8}\,g\tilde{a}^2 \tag{29}$$

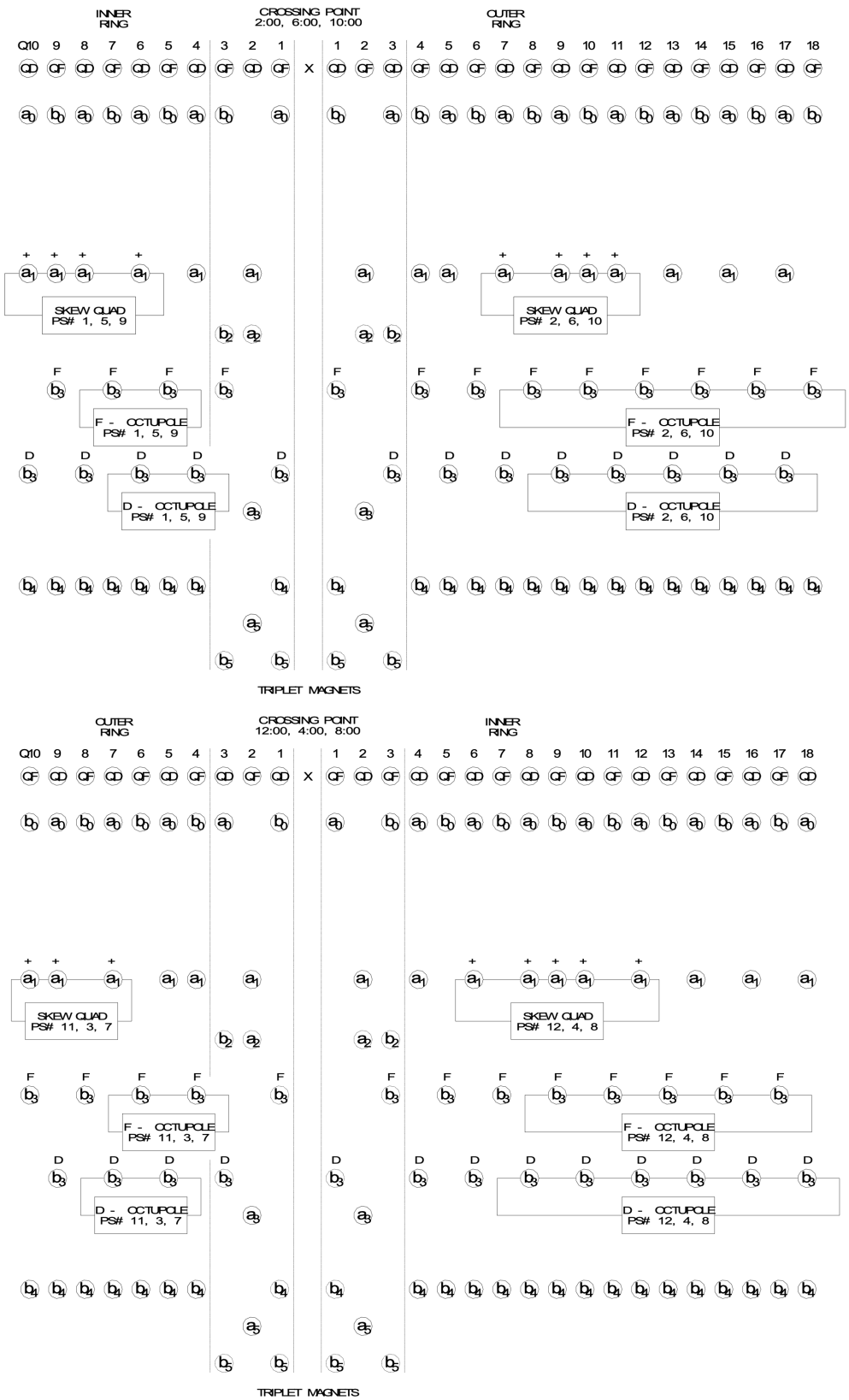


Figure 3: Octupoles and their power supplies in RHIC. Top: IRs 2, 6 and 10. Bottom: IRs 4, 8 and 12.

so the tune

$$Q \;=\; Q_0 \;+\; \frac{\langle \Delta\phi \rangle}{2\pi} \tag{30}$$

changes quadratically with amplitude according to

$$Q \;=\; Q_0 \;+\; \frac{3}{16\pi}\, g\tilde{a}^2 \tag{31}$$

or linearly with action like

$$Q \;=\; Q_0 \;+\; \frac{3}{8\pi}\, gJ \tag{32}$$

The linear rate of change of Q with respect to J is quantified by the horizontal detuning coefficient

$$\kappa\,[\mathrm{m}^{-1}] \;\equiv\; \frac{dQ}{dJ} \tag{33}$$

which is

$$\kappa \;=\; \frac{3}{8\pi}\, g \tag{34}$$

for a single octupole.

Thus the detuning coefficient due to a single octupole is

$$\kappa \;=\; \frac{\beta^2}{16\pi}\, K3.L \tag{35}$$

Performing a double sum over all octupoles driven by all power supplies gives

$$\kappa \;=\; \frac{1}{16\pi} \sum_{\text{supplies}} K3.L \left(\sum_{\text{octupoles}} \beta^2 \right) \tag{36}$$

where β is the horizontal Twiss function, and all octupoles have the same length L.

2.2 Detuning coefficient ranges in both planes

Except for this subsection, this note ignores vertical phase space, and so horizontal and vertical subscripts x or y are usually unnecessary. For completeness, it is natural to briefly discuss the other two detuning coefficients, and to estimate their strength ranges in both RHIC and HSR.

In octupole-dominated optics the horizontal and vertical tunes depend on the two actions like

$$\begin{aligned} Q_x(J_x, J_y) &= Q_{x0} \;+\; \kappa_{xx} J_x \;+\; \kappa_{xy} J_y \\ Q_y(J_x, J_y) &= Q_{y0} \;+\; \kappa_{xy} J_x \;+\; \kappa_{yy} J_y \end{aligned} \tag{37}$$

where the three independent detuning coefficients are

$$\begin{aligned} \kappa_{xx} &= \frac{1}{16\pi} \sum_{\text{supplies}} K3.L \left(\sum_{\text{octupoles}} \beta_x^2 \right) \\ \kappa_{xy} &= \frac{-1}{8\pi} \sum_{\text{supplies}} K3.L \left(\sum_{\text{octupoles}} \beta_x \beta_y \right) \\ \kappa_{yy} &= \frac{1}{16\pi} \sum_{\text{supplies}} K3.L \left(\sum_{\text{octupoles}} \beta_y^2 \right) \end{aligned} \tag{38}$$

in an extension of Equation 36. Simulations using the code Jenny [13] confirm these equations, by comparing the quantitative prediction of the double sums with observations by tracking.

Accel.	Energy & optics	Octupole count	Octupole sums			Detuning coefficient ranges		
			$\sum \beta_x^2$ $10^6\mathrm{m}^2$	$\sum \beta_x \beta_y$ $10^6\mathrm{m}^2$	$\sum \beta_y^2$ $10^6\mathrm{m}^2$	κ_{xx} $10^3\mathrm{m}^{-1}$	κ_{xy} $10^3\mathrm{m}^{-1}$	κ_{yy} $10^3\mathrm{m}^{-1}$
RHIC	injection	90	0.106	0.047	0.103	$\pm$94.9	$\pm$84.2	$\pm$92.3
	storage		0.115	0.050	0.108	$\pm$9.3	$\pm$8.1	$\pm$8.8
HSR	injection	137	0.200	0.116	0.321	$\pm$179.1	$\pm$207.8	$\pm$287.5
	storage		0.243	0.148	0.362	$\pm$19.7	$\pm$24.0	$\pm$29.4

Table 3: RHIC and HSR detuning coefficient ranges. The HSR injection and storage optics are hi-n-inj-101723-proton.bmad and hi-n/275-10-collision/hsr.bmad, with the layout git#17e7f5e69c010f93d5be9cf027e71bec2495beed. The RHIC optics are derived from the Au23-100GeV-e0 lattices.

The octupole sums recorded in Table 3 are positive definite, while the power supply ranges quoted in Equation 25 are bipolar, and so the range of available detuning coefficients in Table 3 are also bipolar. The 3 detuning coefficients are not independent, and so (for example) the peak positive values of κ_{xx} and κ_{xy} can not be reached simultaneously, because of the minus sign in Equation 38. The octupole count in RHIC includes only the 90 octupoles that are powered, ignoring the 11 octupoles per IR that Figure 3 shows are un-powered. The count in the HSR is larger than in RHIC, despite the 19 octupoles that have been removed from IR2 and IR6, because it assumes that all octupoles are powered.

3 Motion close to the 1/4 resonance

Assume that the horizontal resonance of interest for RIJ studies has $N = 4$, so all particles have a tune

$$Q \approx \frac{P}{N} \tag{39}$$

Strictly speaking the integer P is much larger than N, because the integer part of the tune is large. Often the integer tune can be ignored, for example when measurements are made only at a single observation point, once per turn. In that spirit P is taken to be 1 for the RIJ scheme, so that the fractional tune is

$$Q \approx 0.25 \tag{40}$$

It is also assumed that the dominant nonlinear magnets are octupoles. It is possible that the most useful resonance will turn out to have $N = 5$, driven by decapoles, by sextupoles (as in the E778 experiment [14]), or by both. The following development is readily modified for $N \neq 4$, if necessary. It can also be extended from one to two transverse dimensions, if necessary [14, 15].

3.1 One-turn motion

The one-turn discrete Hamiltonian for octupole-dominated motion in action-angle space (J, ϕ) is

$$H_1 = 2\pi Q_0 J + V_{40} J^2 + \sum_{k=2,4} V_{4k} J^2 \sin(k\phi + \phi_{4k}) \tag{41}$$

where V_{40}, V_{42}, and V_{44} are constant coefficients [14]. This Hamiltonian represents one-turn *difference* motion – not differential motion – through the equations

$$\begin{aligned} \Delta\phi &= \frac{\partial H_1}{\partial J} \\ \Delta J &= -\frac{\partial H_1}{\partial \phi} \end{aligned} \tag{42}$$

that are first order in octupole strength. This motion is not small, since for example

$$\Delta\phi = \phi_{n+1} - \phi_n \approx 2\pi Q_0 \approx \frac{\pi}{2} \tag{43}$$

from one turn to the next. Consequently the numerical value of H_1 is *not* in general close to being a constant of the motion. It is usually *not* possible to intuit the motion by drawing contours of $H_1(J, \phi)$ in action-angle space.

3.2 Four-turn motion

The four-turn phase advance is large, with

$$\Delta\phi = \phi_{n+4} - \phi_n \approx 4 \times 2\pi Q_0 \approx 2\pi \tag{44}$$

but after a co-ordinate transformation from ϕ to ψ, where

$$\psi_n = \phi_n - n\left(\frac{2\pi}{N}\right) = \phi_n - n\left(\frac{\pi}{2}\right) \tag{45}$$

then the four-turn phase advance is small, since

$$\Delta\psi = \psi_{n+4} - \psi_n \approx 4 \times 2\pi \left(Q_0 - \frac{1}{4}\right) \approx 0 \tag{46}$$

The four-turn motion in (J,ψ) action-angle space is described by the Kobayashi Hamiltonian [14, 16]

$$H_4 \;=\; 2\pi\left(Q_0-\frac{1}{4}\right)\,J \;+\; V_{40}\,J^2 \;+\; \frac{1}{4}\sum_{t=0}^{3}\sum_{k=2,4} V_{4k}J^2\sin(k(\psi+2\pi Q_0 t)+\psi_{4k}) \tag{47}$$

where the sum in t counts through four turns. The net four-turn motion is then

$$\begin{aligned}\Delta\psi \;&=\; \;\;\;4\,\frac{\partial H_4}{\partial J}\\ \Delta J \;&=\; -\;4\,\frac{\partial H_4}{\partial \psi}\end{aligned} \tag{48}$$

A map of the contours of H_4 in (J,ψ) space restores a graphical understanding of the near-resonant motion, because its numerical value is an approximate constant of the motion.

Although the range of ψ is still broad

$$-\infty \;<\; \psi \;<\; \infty \tag{49}$$

it is convenient to plot the four-turn motion $(J,\psi)_{4n}$ [or $(a,\psi)_{4n}$ or $(\tilde{a},\psi)_{4n}$] within the restricted range

$$0 \;<\; \psi_{restricted} \;<\; 2\pi \tag{50}$$

This achieved by defining the plotted phase to be

$$\psi_{restricted} \;\equiv\; \psi - M(2\pi) \tag{51}$$

where M is an integer that may be negative.

The outer sum in Equation 47 is removed by using the trigonometric identity

$$\sum_{t=0}^{3}\sin\left(A+Bt\right) \;\equiv\; \frac{\sin\left(2B\right)}{\sin\left(B/2\right)}\,\sin\left(A+2B\right) \tag{52}$$

so that

$$H_4 \;=\; 2\pi\left(Q_0-\frac{1}{4}\right)\,J \;+\; V_{40}\,J^2 \;+\; \sum_{k=2,4} V_{44k}J^2\sin(k\psi+\psi_{44k}) \tag{53}$$

where

$$V_{44k} \;\equiv\; \frac{\sin\left(4k\pi Q_0\right)}{4\,\sin\left(k\pi Q_0\right)}\,V_{4k} \tag{54}$$

and

$$\psi_{44k} \;=\; \phi_{4k}+4k\pi Q_0 \tag{55}$$

An important property of Equation 54 is that

$$\begin{aligned}V_{44k} \;&\approx\; V_{4k} \qquad \text{if} \quad \text{mod}\;(k,4)=0\\ V_{44k} \;&\ll\; V_{4k} \qquad \text{if} \quad \text{mod}\;(k,4)\neq 0\end{aligned} \tag{56}$$

to a good approximation, provided that

$$\left|Q_0-\frac{1}{4}\right| \;\ll\; \frac{1}{\pi} \tag{57}$$

so that

$$\begin{aligned}V_{444} \;&\approx\; V_{44}\\ V_{442} \;&\approx\; 0\end{aligned} \tag{58}$$

After substitution into Equation 53 the general four-turn Kobayashi Hamiltonian in (J,ψ) space becomes

$$H_4(J,\psi) \;=\; 2\pi\Delta Q\,J \;+\; V_{40}\,J^2 \;+\; V_{44}\,J^2\sin(4\psi+\psi_{444}) \tag{59}$$

where the shorthand notation

$$\Delta Q \;=\; Q_0 - \frac{1}{4} \tag{60}$$

is introduced for convenience. There are only 4 control parameters: $\Delta Q, V_{40}, V_{44}$, and ψ_{444}. When it is also assumed for convenience, below, that

$$\psi_{444} \;=\; \pi/2 \tag{61}$$

so that

$$\sin(4\psi + \psi_{444}) \;=\; \cos(4\psi) \tag{62}$$

then the four-turn Kobayashi Hamiltonian in (J, ψ) space is further simplified, becoming

$$H_4(J,\psi) \;=\; 2\pi\Delta Q\, J \;+\; V_{40}\, J^2 \;+\; V_{44}\, J^2 \cos(4\psi) \tag{63}$$

with only 3 control parameters: $\Delta Q, V_{40}$, and V_{44}. (General values of ψ_{444} are considered later, in Section 4.)

3.3 Four-turn detuning

The four-turn phase advance in ψ is found by differentiating $H_4(J,\psi)$ with respect to J (see Equation 48), so that

$$\psi_{n+4} \;-\; \psi_n \;=\; 4\left(2\pi\left(Q_0 - \frac{1}{4}\right) \;+\; 2V_{40}J \;+\; 2V_{44}J\cos(4\psi)\right) \tag{64}$$

while the four-turn betatron phase advance in ϕ is

$$\phi_{n+4} \;-\; \phi_n \;=\; 4\,(2\pi Q_0 \;+\; 2V_{40}J \;+\; 2V_{44}J\cos(4\phi)) \tag{65}$$

where the identity

$$\cos(4\psi) \;=\; \cos(4\phi) \tag{66}$$

has been used. In other words the two four-turn phase advances are related through

$$\begin{aligned} \phi_{n+4} \;-\; \phi_n \quad &= \quad 8\pi Q_0 + (\psi_{n+4} \;-\; \psi_n) \\ &\approx \quad 8\pi Q_0 \end{aligned} \tag{67}$$

where the approximation is valid because the rate of advance in ψ is small, by construction.

Tune is the average phase advance per turn (divided by 2π) as turn number goes to infinity,

$$\begin{aligned} Q \quad &\equiv \quad \frac{1}{2\pi}(\phi_{n+t} \;-\; \phi_n) \\ t \quad &\to \quad \infty \end{aligned} \tag{68}$$

or, in this particular case, it is the average phase advance per four-turn (divided by 8π)

$$Q \;\equiv\; \frac{1}{4}\frac{1}{2\pi}\,\langle \phi_{n+4} \;-\; \phi_n \rangle \tag{69}$$

where the average $\langle\rangle$ is taken over very many four-turns. In the non-resonant approximation that J is almost constant then tune is a function of the average action, and substitution of Equation 64 gives

$$Q(J) \;=\; Q_0 \;+\; \frac{1}{\pi}\,\langle V_{40}J \;+\; V_{44}J\cos(4\psi)\rangle \tag{70}$$

Since the ψ values experienced over very many four-turns are evenly distributed in the range 0 to 2π (still in the non-resonant approximation), then

$$\begin{aligned} \langle V_{40}J \rangle \quad &\approx \quad V_{40}J \\ \langle J\cos(4\psi)\rangle \quad &\approx \quad J\,\langle\cos(4\psi)\rangle \;\approx\; 0 \end{aligned} \tag{71}$$

and the tune varies with action simply as

$$Q(J) \;=\; Q_0 \;+\; \frac{V_{40}}{\pi}\, J \tag{72}$$

with a detuning coefficient of

$$\kappa \;=\; \frac{V_{40}}{\pi} \tag{73}$$

Comparing this with Equation 36 shows that the detuning coefficient in the Hamiltonian H_4 is

$$V_{40} \;=\; \pi\kappa \;=\; \frac{1}{16} \sum_{\text{supplies}} K3.L \left(\sum_{\text{octupoles}} \beta^2 \right) \tag{74}$$

where each power supply drives many octupoles, and β is the horizontal Twiss function.

The detuning coefficient V_{40} is a scalar sum over all octupoles – see above. In contrast, the resonance driving coefficient V_{44} is the total length of a vector that is a vector sum over all octupoles – see below.

3.4 The action of the fixed point at the center of a resonance island

The action J_{FP} of the stable fixed point at the heart of a resonance island is found by solving the equation

$$Q(J_{FP}) \;=\; \frac{1}{4} \tag{75}$$

which gives

$$J_{FP} \;=\; -\frac{\pi}{V_{40}}\, \Delta Q \tag{76}$$

after using Equation 72. The corresponding resonance amplitudes in normalized and physical spaces are

$$\begin{aligned} \tilde{a}_{FP} \quad &= \quad \sqrt{2J_{FP}} \;=\; \left(-\frac{2\pi}{V_{40}} \Delta Q \right)^{1/2} \\ a_{FP} \quad &= \quad \sqrt{\beta}\, \tilde{a}_{FP} \;=\; \left(-\frac{2\pi\beta}{V_{40}} \Delta Q \right)^{1/2} \end{aligned} \tag{77}$$

where β is the Twiss function at the observation point. Clearly there is no fixed point if Q_0 is on the wrong side of the resonance: V_{40} and ΔQ must have opposite signs.

3.5 Standard map motion around the island center

The average four-turn phase advance is zero when $J = J_{FP}$ at the island center. At actions near J_{FP} each individual four-turn phase advance is approximately

$$\psi_{n+4} \;-\; \psi_n \;\approx\; 8V_{40}(J - J_{FP}) \tag{78}$$

where terms in ψ (which average to zero over time only in the non-resonant approximation) are temporarily ignored. This phase motion is represented by an approximate Hamiltonian

$$H_4(I) \;\approx\; V_{40}\, I^2 \tag{79}$$

where the action offset from the island center

$$I \;=\; J \;-\; J_{FP} \;\ll\; J_{FP} \tag{80}$$

is assumed to be small. So long as the islands are small (so that Equation 80 remains true for all trajectories of interest) it turns out that four-turn motion is well represented by the resonance Hamiltonian

$$H_R(I, \psi) \;=\; V_{40}\, I^2 \;+\; V_{44} J_{FP}^2 \cos(4\psi) \tag{81}$$

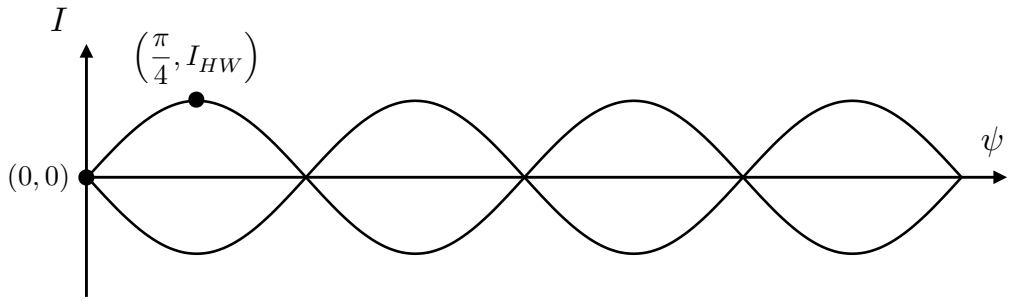


Figure 4: The separatrix contours of a 4-island chain with the resonance Hamiltonian given by Equation 81. Comparing H_R values at $(\psi, I) = (0,0)$ and $(\pi/4, I_{HW})$ enables the calculation of the island half-width I_{HW}.

This is identical (within constants) to the "standard map" Hamiltonian that describes a pendulum, RF buckets, and many other nonlinear systems.

There are 4 stable and 4 unstable fixed points at the local minima and maxima of H_R, with

$$\begin{aligned} I_{FP} &= 0 \\ \cos(4\psi_{FP}) &= +1 \qquad \text{unstable} \\ \cos(4\psi_{FP}) &= -1 \qquad \text{stable} \end{aligned} \tag{82}$$

where V_{40} and V_{44} are assumed to have the same sign. The resonance island centers therefore have fixed point phases at

$$\psi_{FP} \;=\; \frac{\pi}{4},\; \frac{3\pi}{4},\; \frac{5\pi}{4},\; \frac{7\pi}{4} \tag{83}$$

as illustrated in Figure 4. Stable fixed points become unstable, and vice versa, if V_{40} and V_{44} have different signs.

3.6 Resonance island width

Unstable motion launched very slightly above the unstable fixed point at

$$(I, \psi) \;=\; (0,0) \tag{84}$$

reaches all values of phase ψ, traveling just outside the separatrix contours that skirt the island chain. This is illustrated in Figure 4, where it is implicitly assumed that V_{40} and V_{44} have the same sign. The island half width I_{HW} is calculated by equating the values of H_R on the separatrix at the stable and unstable fixed point phases

$$H_R(0,0) \;=\; H_R\left(I_{HW}, \frac{\pi}{4}\right) \tag{85}$$

Substitution into Equation 81 shows that

$$V_{44} J_{FP}^2 \;=\; V_{40} I_{HW}^2 \;-\; V_{44} J_{FP}^2 \tag{86}$$

and leads to the prediction that the island half-width

$$I_{HW} \;=\; \left(\frac{2V_{44}}{V_{40}}\right)^{1/2} \cdot J_{FP} \tag{87}$$

is linear in J_{FP}. Clearly the ratio V_{44}/V_{40} is very important! Using Equation 76 the island half width becomes

$$I_{HW} \;=\; \pi \left|\frac{2V_{44}}{V_{40}^3}\right|^{1/2} |\Delta Q| \tag{88}$$

in terms of the 3 control parameters, $\Delta Q, V_{40}$, and V_{44}, no matter what their signs (except that ΔQ and V_{40} have opposite signs). In terms of the detuning coefficient κ this becomes

$$I_{HW} \;=\; \left|\frac{2V_{44}}{\pi\kappa^3}\right|^{1/2} |\Delta Q| \tag{89}$$

Continuing to assume that the islands are relatively small

$$I_{HW} \;\ll\; J_{FP} \tag{90}$$

then it is reasonable to approximate the normalized and physical space *half* widths to be

$$\begin{aligned} \tilde{a}_{HW} &\approx \left(\frac{1}{2J_{FP}}\right)^{1/2} \cdot I_{HW} \\ a_{HW} &\approx \left(\frac{\beta}{2J_{FP}}\right)^{1/2} \cdot I_{HW} \end{aligned} \tag{91}$$

respectively, where β is the Twiss function at the observation point.

3.7 Resonance island tunes

Four-turn difference motion near the resonance is described by differentiating H_R

$$\begin{aligned} \psi_{n+4} - \psi_n &= 4\,\frac{\partial H_R}{\partial I} \\ I_{n+4} - I_n &= -4\,\frac{\partial H_R}{\partial \psi} \end{aligned} \tag{92}$$

Since this four-turn motion is small (by construction), it is reasonable to use a differential approximation

$$\begin{aligned} \frac{d\psi}{dt} &= 2V_{40} \cdot I \\ \frac{dI}{dt} &= 4V_{44}J_{FP}^2 \cdot \sin(4\psi) \end{aligned} \tag{93}$$

in which time t is continuous – it is not an integer, but increases by 4.0 every 4 turns.

Small oscillations close to a stable fixed point at phase ψ_{FP}, with

$$\Delta\psi \;=\; \psi - \psi_{FP} \;\ll\; 1 \tag{94}$$

allow the approximation

$$\sin(4\psi) \;\approx\; -4\Delta\psi \tag{95}$$

to be made. This leads to two first order linear differential equations of motion

$$\begin{aligned} \frac{d(\Delta\psi)}{dt} &= 2V_{40} \cdot I \\ \frac{dI}{dt} &= -16V_{44}J_{FP}^2 \cdot \Delta\psi \end{aligned} \tag{96}$$

Since

$$\frac{d^2I}{dt^2} \;=\; -16V_{44}J_{FP}^2 \cdot \frac{d(\Delta\psi)}{dt} \tag{97}$$

then these two first order equations lead to a single second order differential equation in I

$$\frac{d^2I}{dt^2} \;+\; (32V_{40}V_{44}J_{FP}^2) \cdot I \;=\; 0 \tag{98}$$

that describes simple harmonic motion, with a solution

$$\begin{aligned} I &= a_I \cos(2\pi Q_I t) \\ \psi - \psi_{FP} &= a_\psi \sin(2\pi Q_I t) \end{aligned} \tag{99}$$

Differentiating Equation 99 twice gives

$$\frac{d^2 I}{dt^2} + (2\pi\, Q_I)^2 . I = 0 \tag{100}$$

showing that the island tune is

$$Q_I = \frac{1}{\pi} (8\, V_{40} . V_{44})^{1/2} \cdot J_{FP} \tag{101}$$

Here, as before, it is assumed that V_{40} and V_{44} have the same sign. This predicts that Q_I is linear in J_{FP} as ΔQ is scanned at fixed octupole strengths.

Using Equation 76 to eliminate J_{FP} the island tune becomes

$$Q_I = \left| \frac{8\, V_{44}}{V_{40}} \right|^{1/2} \cdot |\Delta Q| \tag{102}$$

in terms of the 3 control parameters, $\Delta Q, V_{40}$, and V_{44}, no matter what their signs (except that ΔQ and V_{40} have opposite signs). Alternatively, in terms of the detuning coefficient κ this becomes

$$Q_I = \left| \frac{8\, V_{44}}{\pi \kappa} \right|^{1/2} \cdot |\Delta Q| \tag{103}$$

Insofar as V_{40} and V_{44} can be tuned independently, the former controls the detuning and the latter controls the strength of the island.

Equation 103 [or 89] can be inverted to deliver V_{44} as a function of $(\Delta Q, Q_I, \kappa)$ [or $(\Delta Q, I_{HW}, \kappa)$]. In the same spirit that V_{40} can be considered to be a knob that delivers the more fundamental detuning quantity κ, the more fundamental complete set of control variables may be considered to be $(\Delta Q, Q_I, \kappa)$ – two tunes and one tune slope.

4 Evaluating the resonance driving vector $\bar{V}_{44}$

The action changes over four turns by

$$\Delta J \;=\; -4\,\frac{\partial H_4}{\partial \psi} \tag{104}$$

according to Equation 48, where the action angle co-ordinates at the observation point are (J, ψ) at the beginning of the four turns [14, 15]. Differentiating the general four-turn Hamiltonian H_4 in Equation 59 shows that the change in action over four turns is

$$\Delta J \;=\; -16\,V_{44}\,J^2\cos(4\psi + \psi_{444}) \tag{105}$$

Given a set of octupoles of different normalized strengths g [m^{-1}] at locations with horizontal betatron phases θ downstream of the observation point, what are the values of V_{44} and ψ_{444}?

4.1 One octupole, one turn

Figure 5 illustrates how one octupole changes the action from J_0 to J_1 on the first of four turns. The normalized displacement and angle just before the kick are

$$\begin{aligned} \tilde{x}_0 &= \tilde{a}_0\,\sin(\psi_0+\theta) \\ \tilde{x}'_0 &= \tilde{a}_0\,\cos(\psi_0+\theta) \end{aligned} \tag{106}$$

and just after are

$$\begin{aligned} \tilde{x}_1 &= \tilde{x}_0 \\ \tilde{x}'_1 &= \tilde{x}'_0 \;-\; g\,\tilde{x}_0^3 \end{aligned} \tag{107}$$

with a new normalized amplitude of

$$\tilde{a}_1 \;=\; \sqrt{\tilde{x}_1^2 + \tilde{x'}_1^2} \tag{108}$$

Careful consideration of Figure 5 shows that the change in normalized amplitude is

$$\Delta\tilde{a} \;=\; -g\,\tilde{a}_0^3.\sin^3(\psi_0+\theta)\cos(\psi_0+\theta) \tag{109}$$

to first order in octupole strength g, with a corresponding change in action of

$$\Delta J \;=\; \left(\frac{dJ}{d\tilde{a}}\right).\Delta\tilde{a} \;=\; \tilde{a}.\Delta\tilde{a} \tag{110}$$

since

$$J \;=\; \frac{1}{2}\tilde{a}^2 \tag{111}$$

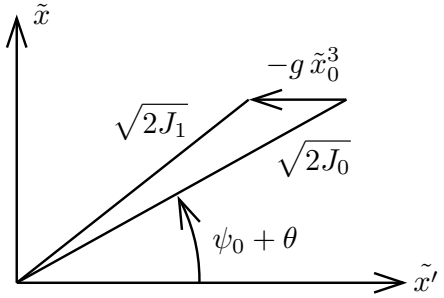


Figure 5: Change of action in the first turn of a trajectory launched with (J_0, ψ_0), due to one octupole of strength g at a location with a phase advance of θ downstream from the observation point.

In purely action angle co-ordinates the one-turn change in action is therefore

$$\Delta J \;=\; -4gJ_0^2.\sin^3(\psi_0+\theta)\cos(\psi_0+\theta) \tag{112}$$

to first order in g. This is simplified into harmonics

$$\Delta J \;=\; -4g\,J_0^2.\left[\frac{1}{4}\sin(2(\psi_0+\theta))-\frac{1}{8}\sin(4(\psi_0+\theta))\right] \tag{113}$$

by applying the identity

$$\sin^3(A)\cos(A) \;\equiv\; \frac{1}{4}\sin(2A)-\frac{1}{8}\sin(4A) \tag{114}$$

Nonetheless, we're interested in the change in action due to many octupoles over four turns, not due to one octupole over one turn.

4.2 Many octupoles, four turns

The net change in action over four turns, from $n=0$ to 3, is

$$\Delta J \;=\; -4g\,J_0^2\sum_{n=0}^{3}\left[\frac{1}{4}\sin(2(\psi_0+\theta+n\pi/2))-\frac{1}{8}\sin(4(\psi_0+\theta+n\pi/2))\right] \tag{115}$$

since the net phase advance from the observation point to an octupole increases by (approximately) $\pi/2$ per turn. This is simplified by recognizing that

$$\begin{aligned}\sum_{n=0}^{3}\sin(2(A+n\pi/2)) &= 0 \\ \sum_{n=0}^{3}\sin(4(A+n\pi/2)) &= 4\sin(4A)\end{aligned} \tag{116}$$

so that

$$\Delta J \;=\; 2g\,J^2.\sin(4\psi_0+4\theta) \tag{117}$$

over four turns, always assuming that g is small and the tune Q_0 is very close to one quarter. Comparing Equation 105 to Equation 117, using the identity

$$\cos A \;\equiv\; \sin(A+\pi/2) \tag{118}$$

and referring to Equation 20 shows that

$$\begin{aligned}V_{44} &= -\frac{g}{8} = -\frac{\beta^2}{48}(K3.L) \\ \psi_{444} &= 4\theta-\pi/2\end{aligned} \tag{119}$$

for a single octupole of normalized strength g at a horizontal phase θ downstream of the observation point.

Vectors must be added when many octupoles are present. The resonance driving vector

$$\vec{V}_{44} \;\equiv\; V_{44}\begin{pmatrix}\sin(\psi_{444})\\ \cos(\psi_{444})\end{pmatrix} \;=\; -\frac{1}{48}\sum_{\text{supplies}}K3.L\left(\sum_{\text{octupoles}}\beta^2\begin{pmatrix}\sin(4\theta-\pi/2)\\ \cos(4\theta-\pi/2)\end{pmatrix}\right) \tag{120}$$

is found by summing over all octupoles driven by all power supplies. Finding the length and angle of $\vec{V}_{44}$ is the last step in evaluating V_{44} and ψ_{444}. The octupole power supply strengths $K3.L$ are played off against each other to deliver desirable values of V_{44} and ψ_{444}, during the design of the resonance islands – their phase locations, their widths, and their island tune Q_I.

4.3 Resonance driving sensitivity vectors $\vec{S}_{PS}$

The resonance driving vector is conveniently rewritten in terms of resonance driving sensitivity vectors as

$$\vec{V}_{44} \;=\; \sum_{\text{supplies}} (K3.L)\, \vec{S}_{PS} \tag{121}$$

in order to focus on the power supply strengths $K3.L$. The sensitivity vector for each power supply

$$\vec{S}_{PS} \;=\; S_{PS} \begin{pmatrix} \sin(\psi_{PS}) \\ \cos(\psi_{PS}) \end{pmatrix} \;=\; \sum_{\text{octupoles}} \frac{-\beta^2}{48} \begin{pmatrix} \sin(4\theta - \pi/2) \\ \cos(4\theta - \pi/2) \end{pmatrix} \tag{122}$$

is found by summing over all the octupoles that it drives. Table 4 quantifies the lengths and angles of all 24 octupole island sensitivity vectors. The F-octupole power supplies (driving octupoles at locations with large values of $\beta \approx 50$ m) are much more effective than the D-octupole power supplies (with $\beta \approx 10$ m).

Octupole power supply name	**Island sensitivity vector $\vec{S}_{44}$**	
	S_{PS} [m^{-1}]	ψ_{PS} [rad]
F-octupoles		
bi1-octf	86.762994	3.747207
bo2-octf	185.812956	1.130666
bo3-octf	43.629200	0.558871
bi4-octf	170.830969	3.591007
bi5-octf	90.083822	2.172908
bo6-octf	185.455997	-0.480507
bo7-octf	45.648757	-1.115900
bi8-octf	169.933786	1.440566
bi9-octf	86.459064	-0.123419
bo10-octf	185.530087	3.507139
bo11-octf	45.164195	2.848658
bi12-octf	170.999513	-0.905556
D-octupoles		
bi1-octd	8.905996	3.770398
bo2-octd	11.104991	4.516711
bo3-octd	4.889683	-1.392257
bi4-octd	6.796010	0.328991
bi5-octd	9.257270	2.256010
bo6-octd	11.117783	2.916802
bo7-octd	4.820819	3.223661
bi8-octd	6.313916	4.486214
bi9-octd	8.374727	-0.082642
bo10-octd	10.990071	0.609628
bo11-octd	4.751588	0.882171
bi12-octd	6.289794	2.115453

Table 4: Octupole power supply island sensitivities $\vec{S}_{PS}$ in stepstone Au23-100GeV-e0::injection of the Blue injection lattice used during 100 GeV/u gold operations in 2023. Even the weakest F-octupole family is about 4 times stronger than the strongest D-octupole family.

Figure 6 shows all 12 F-octupole family island sensitivity vectors, but no D-octupole vectors. The vectors in odd-numbered RHIC sectors are significantly shorter than those in even-numbered sectors. Red vectors, labeled bA, bB, and bC, represent the total effect of pairs of power supplies – bo2 and bi8, bi4 and bo10, and bo6 and bi12 – (which have vectors that are close to parallel) when they are powered at exactly the same strength. These three 'effective' power supplies are spaced in phase by approximately 120 degrees, as listed in Table 5, showing that all net phases are accessible.

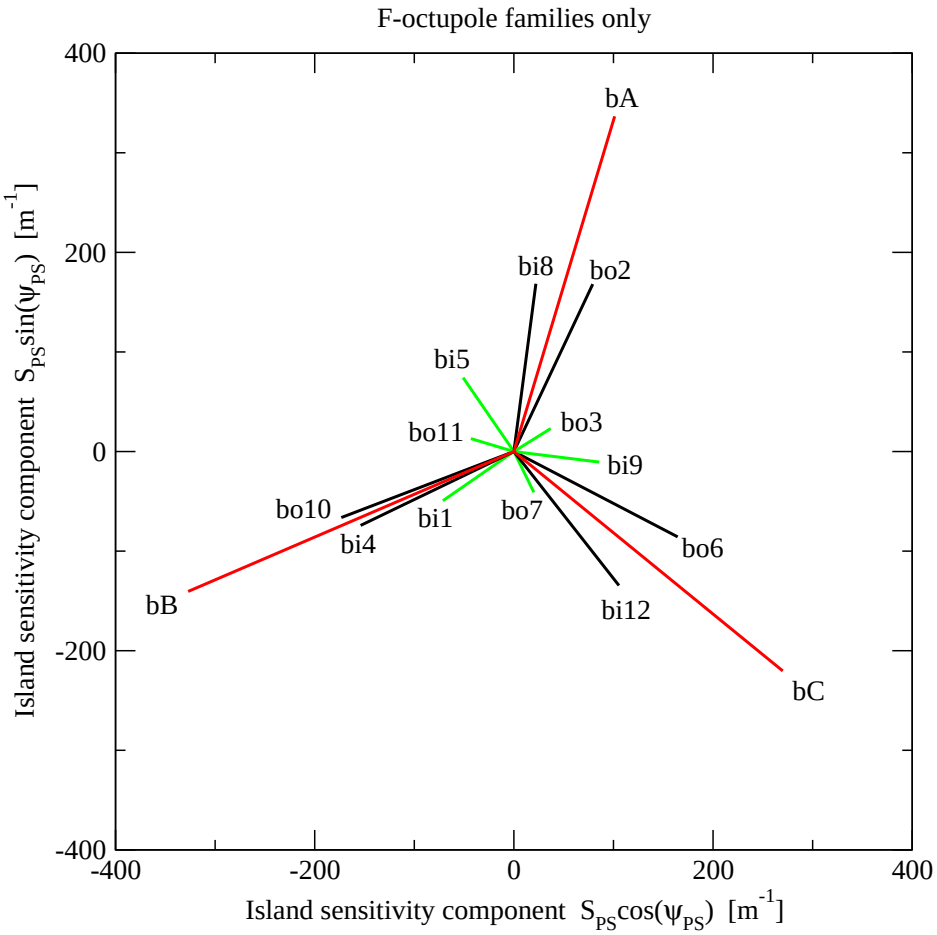


Figure 6: Octupole power supply island sensitivity vectors $\vec{S}_{PS}$ in stepstone Au23-100GeV-e0::injection of the Blue injection lattice used during 100 GeV/u gold operations in 2023. Only the F-octupole vectors are shown: they are much longer than the D-octupole vectors (see Table 4). Green vectors represent the relatively small sensitivities in odd-numbered RHIC sectors. Red vectors represent the 'effective' power supplies bA, bB, and bC.

Effective power supply name	**Island sensitivity vector $\vec{S}_{44}$**	
	S_{PS} [m^{-1}]	ψ_{PS} [rad]
bA	351.5	1.2786
bB	356.0	3.5473
bC	348.4	5.5989

Table 5: Island sensitivities $\vec{S}_{PS}$ for the three effective octupole power supplies bA, bB, and bC in stepstone Au23-100GeV-e0::injection of the Blue injection lattice used during 100 GeV/u gold operations in FY23.

5 Ramping and modulating the tune

Sinusoidal tune modulation is parameterized in general by q and Q_M, where the (zero action) betatron tune varies with time like

$$Q_0 \;=\; Q_{00} \;+\; q\,\sin(2\pi\,Q_M t) \tag{123}$$

Here q is the tune modulation amplitude or depth, Q_M is the tune modulation tune, and t is turn number. This section discusses the radically different dynamical responses in different partitions of tune modulation parameter space (q, Q_M), displaying

1. Amplitude modulation
2. Frequency (or phase) modulation
3. Strong synchrobetatron sidebands
4. Widespread chaos

Tune modulation occurs naturally for a particle oscillating longitudinally with an off-momentum amplitude of $\hat{\delta}$ when the chromaticity χ is non-zero. In that case the amplitude and tune are

$$\begin{aligned} q &= \chi\,\hat{\delta} \\ Q_M &= Q_s \end{aligned} \tag{124}$$

where Q_s is the synchrotron tune. Tune modulation can also be introduced externally as part of an experimental technique to measure island tunes, as discussed in Section 6. For example, sinusoidally driven transition jump quads can be used to introduce tune modulation over a limited range of q and Q_M, as discussed in Section 1.3.

5.1 Slow linear tune ramps

If the tune is ramped *slowly* at a constant rate of $\dot{Q}$, so that on turn t

$$Q_0 \;=\; Q_{00} \;+\; \dot{Q}\,t \tag{125}$$

then the four-turn resonance Hamiltonian of Equation 81 becomes

$$H_R(I,\psi) \;=\; 2\pi\dot{Q}t\,I \;+\; V_{40}\,I^2 \;+\; V_{44}J_{FP}^2\,\cos(4\psi) \tag{126}$$

where J_{FP} (the action of the island center at $t = 0$) is a constant [14]. The slowly moving fixed point action offset I_{FP} is found at any t by solving for

$$\frac{\partial H_R}{\partial I} \;=\; 0 \tag{127}$$

so that

$$I_{FP} \;=\; -\left(\frac{\pi\dot{Q}}{V_{40}}\right)\,t \;\equiv\; -\zeta\,t \tag{128}$$

The explicit time dependence in the Hamiltonian is reduced to second order in the small quantity ζ by performing a canonical transformation from (I,ψ) to $(\bar{I},\bar{\psi})$ [17], using the generating function

$$W_1(I,\bar{\psi},t) \;=\; I\,\bar{\psi} \;+\; \zeta\,t\,\bar{\psi} \tag{129}$$

so that

$$\bar{I} \;\equiv\; \partial W_1/\partial\bar{\psi} \;=\; I \;+\; \zeta\,t \tag{130}$$

$$\psi \;\equiv\; \partial W_1/\partial I \;=\; \bar{\psi} \tag{131}$$

$$\bar{H}_R \;\equiv\; H_R \;+\; \partial W_1/\partial t \;=\; H_R \;+\; \zeta\bar{\psi}$$

The new action variable $\bar{I}$ is the action displacement from the moving fixed point, while the angle variable is unchanged.

The new Hamiltonian is no longer periodic in the angle $\bar{\psi}$

$$\bar{H}_R \;=\; V_{40}\,\bar{I}^2 \;+\; V_{44}J_{FP}^2\,\cos(4\bar{\psi}) \;+\; \zeta\bar{\psi} - V_{40}\zeta^2 t^2 \tag{132}$$

and only has stable fixed points if there is a solution to

$$\frac{\partial \bar{H}_R}{\partial \bar{\psi}} \;=\; 0 \tag{133}$$

that is, if

$$\left|\dot{Q}\right| \;<\; \frac{4}{\pi}V_{40}V_{44}J_{FP}^2 \tag{134}$$

This is analogous to longitudinal motion during acceleration, in which the stable RF buckets shrink and become shaped like tear drops as the acceleration rate increases, or even disappear all together.

5.2 Slow sinusoidal tune modulation

If the tune modulation is slow enough

$$Q_M \;\ll\; Q_I \tag{135}$$

then sinusoidal oscillations are equivalent to adiabatically varying the linear ramp rate in the range

$$-\,2\pi\,q\,Q_M \;<\; \dot{Q} \;=\; \frac{dQ}{dt} \;<\; 2\pi\,q\,Q_M \tag{136}$$

Substituting these extreme values of $\dot{Q}$ into Equation 134 and comparing with Equation 101 shows that particles are only adiabatically trapped in resonance islands of order N if

$$q\,Q_M \;<\; \frac{Q_I^2}{N} \tag{137}$$

Resonance islands in this (weak and slow) partition of tune modulation parameter space move to larger and smaller amplitudes at constant phase – displaying amplitude modulation.

5.3 Rapid sinusoidal tune modulation

The response to rapid sinusoidal tune modulation is modeled, first, by explicitly including it in a time-dependent version of the time-independent resonance Hamiltonian of Equation 81

$$H_R(I,\psi) \;=\; 2\pi\,q\,\sin(2\pi Q_M t)\,I \;+\; V_{40}\,I^2 \;+\; V_{44}J_{FP}^2\,\cos(4\psi) \tag{138}$$

This Hamiltonian is then canonically transformed using another generating function [17]

$$W_2(I,\bar{\psi},t) \;=\; \bar{\psi}\,I \;+\; \frac{q}{Q_M}\,\cos(2\pi Q_M t)\,I \tag{139}$$

so that

$$\begin{aligned}
\bar{I} \;&=\; I && (140)\\
\psi \;&=\; \bar{\psi} \;+\; \frac{q}{Q_M}\,\cos(2\pi Q_M t) && (141)\\
\bar{H}_R \;&=\; H_R \;-\; 2\pi\,q\sin(2\pi Q_M t)
\end{aligned}$$

The new action $\bar{I}$ is unchanged, the new angle $\bar{\psi}$ is sinusoidally modulated with respect to the old angle, and the new four-turn resonance Hamiltonian

$$\bar{H}_R(\bar{I},\bar{\psi}) \;=\; V_{40}\,\bar{I}^2 \;+\; V_{44}J_{FP}^2\,\cos\left(4\bar{\psi} \;+\; \frac{4q}{Q_M}\cos(2\pi Q_M\,t)\right) \tag{142}$$

has a tune modulation term inside the cosine argument. When the identity

$$\cos(A \,+\, B\cos(C)) \;=\; \sum_{k=-\infty}^{\infty} J_k(B)\cos(A+kC) \tag{143}$$

is used to introduce an infinite sum over Bessel functions J_k, the Hamiltonian at last displays synchrobetatron behavior

$$\bar{H}_R(\bar{I},\bar{\psi}) \;=\; V_{40}\,\bar{I}^2 \,+\, V_{44}J_{FP}^2 \sum_{k=-\infty}^{\infty} J_k\left(\frac{4q}{Q_M}\right)\cos(4\bar{\psi}+k\,2\pi Q_M t) \tag{144}$$

(Beware the potential for notational confusion – is J an action or a Bessel function?)

If a test particle has an action close to

$$\bar{I}_k \;=\; k\left(\frac{\pi\,Q_M}{4V_{40}}\right) \tag{145}$$

where k is any integer, then the betatron tune is close to the k'th synchrobetatron sideband tune of

$$Q(\bar{I}_k) \;=\; \frac{1}{N} \,+\, k\left(\frac{Q_M}{N}\right) \tag{146}$$

If so, the net phase advance over $N = 4$ *modulation* periods is small. Assuming that the modulation period

$$M \;=\; 1/Q_M \tag{147}$$

is a large integer, then all of the harmonic terms in Equation 144 except one disappear in going to the k'th type of $4M$-turn Hamiltonian,

$$\bar{H}_{4Mk} \;=\; V_{40}\,(\bar{I}-\bar{I}_k)^2 \,+\, V_{44}J_{FP}^2\,.\,J_{-k}\left(\frac{4q}{Q_M}\right)\cos(4\bar{\psi}) \tag{148}$$

due to the same kind of averaging that occurs when deriving the 4-turn Hamiltonian of Equation 59. Just as that Hamiltonian properly describes motion only over every 4 turns, this Hamiltonian $\bar{H}_{4Mk}$ represents synchrobetatron motion over every $4M$ turns. This is the appropriate time span to use in a Poincaré surface of section representation of the motion.

Crucially, the averaging is only valid if not much happens in $4M$ turns – that is, if

$$Q_M \;\gg\; Q_I \tag{149}$$

Resonance islands in this (fast) partition of tune modulation parameter space remain at constant amplitude but oscillate in phase – displaying frequency or phase modulation. This partition may also exhibit multiple strong synchrobetatron island chains, if the amplitude q is large enough – see below.

5.4 Synchrobetatron sidebands and islands

Each 4M-turn Hamiltonian $\bar{H}_{4Mk}$ generates a chain of four synchrobetatron islands – one chain for every integer k. Chains with large enough values of $|k|$ have inconsequentially small islands. Nonetheless sideband islands with non-zero values of k are comparable in size to the primary island chain with $k = 0$ in some parts of tune modulation parameter space (q, Q_M).

Mathematically, the strong suppression of sidebands with too-large values of $|k|$ occurs because of the Bessel function approximations

$$\begin{aligned} J_k(A) \;&\approx\; \left(\tfrac{2}{\pi A}\right)^{1/2}\cos\left(A-\tfrac{k\pi}{2}-\tfrac{\pi}{4}\right) \qquad \text{if} \;\; A > k > 0 \\ &\approx\; 0 \qquad\qquad\qquad\qquad\qquad\qquad\quad \text{if} \;\; A < k \end{aligned} \tag{150}$$

In the case at hand the argument for resonance order N is

$$A \;=\; \frac{Nq}{Q_M} \tag{151}$$

so that the k'th Bessel function is approximated by

$$\begin{aligned} J_k\left(\frac{Nq}{Q_M}\right) &\approx \left(\tfrac{2Q_M}{\pi Nq}\right)^{1/2}\cos\left(\tfrac{Nq}{Q_M}-\tfrac{k\pi}{2}-\tfrac{\pi}{4}\right) \qquad \text{if} \quad \frac{Nq}{Q_M} > |k| \\ &\approx 0 \qquad\qquad\qquad\qquad\qquad\quad \text{if} \quad \frac{Nq}{Q_M} < |k| \end{aligned} \tag{152}$$

Thus, sidebands of positive or negative order k are significant in size only over the range

$$-\frac{Nq}{Q_M} \;<\; k \;<\; \frac{Nq}{Q_M} \tag{153}$$

In particular, only the fundamental $k = 0$ islands are large compared to the other sideband islands if

$$q \;<\; \frac{Q_M}{N} \tag{154}$$

Physically, the motion of a test particle is almost unperturbed if its tune modulation amplitude q is too small for it to periodically sweep across the rational fraction tune (e.g. 1/4) of the primary resonance.

5.5 Synchrobetatron sideband overlap

The half-width of the synchrobetatron islands in sideband chain k

$$I_{HWk} \;=\; \pi\left|J_{-k}\left(\frac{Nq}{Q_M}\right).\frac{2V_{44}}{V_{40}^3}\right|^{1/2}|\Delta Q| \tag{155}$$

is closely related to the half-width without modulation – see Equation 88. When the sidebands are strong the upper approximation in Equation 152 applies, and the islands have a half-width of order

$$I_{HWk} \;\sim\; \pi\left|\frac{2Q_M}{\pi Nq}\right|^{1/4}\left|\frac{2V_{44}}{V_{40}^3}\right|^{1/2}|\Delta Q| \tag{156}$$

after neglecting the cosine factor in the approximation.

Large scale chaos is visible in a Poincaré surface of section when the sidebands overlap – when the action separating two neighboring sidebands

$$\Delta\bar{I}_k \;=\; \frac{\pi\, Q_M}{4V_{40}} \tag{157}$$

(see Equation 145) is smaller than their total width

$$\Delta\bar{I}_k \;<\; I_{HWk} \,+\, I_{HW(k+1)} \tag{158}$$

The approximate condition for sideband overlap and massive chaos becomes

$$Q_M^{3/4}(Nq)^{1/4} \;<\; \frac{4}{\pi^{1/4}}Q_I \tag{159}$$

after using Equation 102 and the approximation of Equation 156.

5.6 Dynamical partitions in tune modulation parameter space

Particle responses are radically different in the four different partitions of tune modulation parameter space (q, Q_M) that are sketched in Figure 7 for resonance order $N = 4$. The three boundaries separating these four partitions

$$\begin{aligned} \left(\frac{q}{Q_I}\right)\quad\left(\frac{Q_M}{Q_I}\right) &= \frac{1}{N} && \text{Amplitude modulation } \leftrightarrow \text{ chaos} \\ \left(\frac{q}{Q_I}\right)\quad\left(\frac{Q_M}{Q_I}\right)^{-1} &= \frac{1}{N} && \text{Phase modulation } \leftrightarrow \text{ strong sidebands} \\ \left(\frac{q}{Q_I}\right)^{1/4}\left(\frac{Q_M}{Q_I}\right)^{3/4} &= \frac{4}{(N\pi)^{1/4}} && \text{Strong sidebands } \leftrightarrow \text{ chaos} \end{aligned} \tag{160}$$

that are derived from Equations 137, 154, and 159 are only approximate. Numerical and beam studies confirm the broad separation of responses into four partitions, but with boundaries that show a significant amount of fine structure [15].

The boundaries of Equation 160 show that the more fundamental parameters are q/Q_I and Q_M/Q_I – the tune modulation parameters scaled by Q_I [18, 14]. These boundaries apply no matter what the resonance source (beam-beam or magnetic), and no matter what the tune modulation source (chromatic or external). The universality of this behavior further emphasizes the crucial role played by the island tune, Q_I.

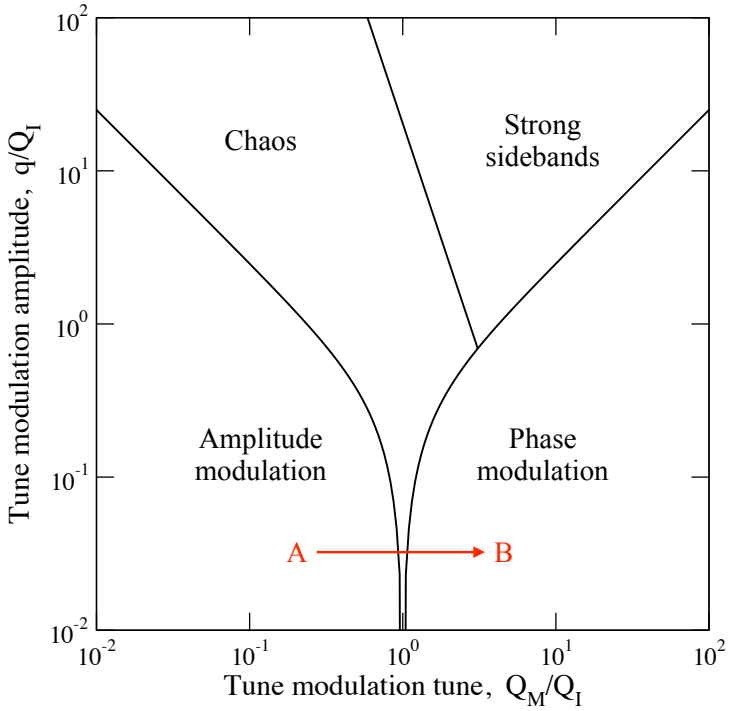


Figure 7: Dynamical partitions in tune modulation parameter space for an $N = 4$ resonance. Equation 160 shows that the more fundamental parameter space $(q/Q_I, Q_M/Q_I)$ is scaled by Q_I, emphasizing the crucial role played by the island tune. Detailed numerical and beam studies show a lot of fine structure – the boundaries are only approximate. The island tune can be measured by chirping an external source of tune modulation, for example scanning from A to B.

The boundaries between dynamical partitions can be explored by first placing beam into a resonance island, and then applying an externally controlled tune modulation. Turn-by-turn Beam Position Monitors observe a "persistent signal" with a strong signal at the resonance tune $1/N$, if much (or all) of the beam is trapped in a resonance island. This persistent signal is destroyed if tune modulation is then turned on with (q, Q_M) parameters in the region labeled "chaos" in Figure 7. The island tune Q_I can then be inferred by recording the parameters at which the signal is lost. Confirming the agreement between resonance strength prediction and beam measurement is a crucial step in evaluating an RIJ scheme for HSR.

For example, the tune modulation frequency Q_M can be chirped across the chaos region at a constant small amplitude

$$q \ll Q_I \tag{161}$$

as illustrated by going from A to B in Figure 7. This has the advantage of requiring only weak AC quadrupoles (or their equivalent) to measure Q_I with significant precision. It also illustrates how dipole or quadrupole power supply ripple harmonics at tunes close to Q_I can introduce chaos, if such resonances are present. Of course, other trajectories in (q, Q_M) space can also destroy a persistent signal and measure Q_I, if convenient.

RHIC currently does not include purpose-built AC quadrupoles that can be used as an external source of tune modulation that can be used to measure island tunes. Some tune modulation capability is provided by re-purposing the transition jump quadrupoles, as discussed in section 1.3.

6 Tune modulation and data reduction techniques

The dynamics of a metastable beam of particles trapped in artificially excited resonance islands were studied in the Tevatron in the late 1980's and early 1990's, as part of the Fermilab E778 nonlinear beam dynamics experiment [15, 19, 20, 21, 22, 23, 24, 25, 26, 27]. Similar studies could be performed in RHIC, to investigate the potential of the RIJ scheme for transition crossing in the HSR.

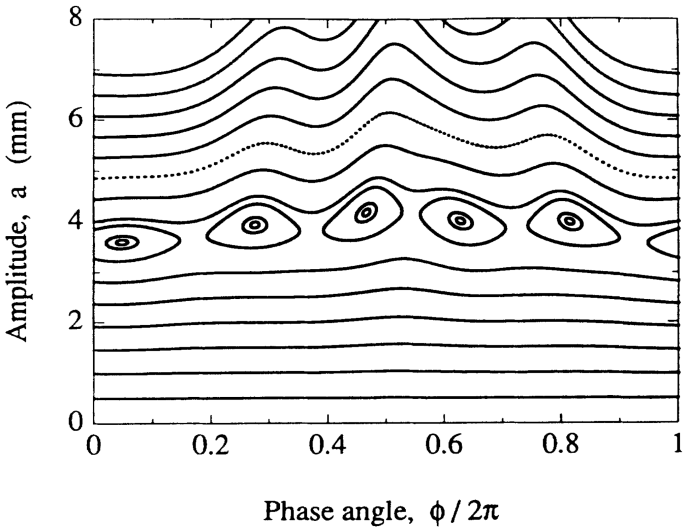


Figure 8: Simulated structure of horizontal phase space in the Tevatron with a tune $Q_x \approx 2/5$, as distorted by fourteen strong sextupoles that drove the $N = 5$ resonance islands [27].

The structure of horizontal phase space in one of the many configurations of the E778 experiment is shown in Figure 8. In this case 14 of the Tevatron sextupoles were powered much more strongly than the other chromaticity sextupoles, although with no net change to the horizontal and vertical chromaticities. These sextupoles drove $N = 5$ resonance islands when the base horizontal tune Q_0 was slightly less than $2/5$, because the horizontal tune increased with amplitude a (in mm) according to

$$Q_x \;=\; Q_0 \;+\; 0.000237\, a^2 \tag{162}$$

Every 120 seconds a single bunch of about 10^{10} protons was injected into the Tevatron and stored, enabling data to be taken repeatedly with a 2 minute cycle time. The beam was kicked horizontally with a typical amplitude of around 4 mm after about 10 seconds, when the injection transients had died down. Most of the beam was trapped in one of the 5 resonance islands that are located with horizontal phases of approximately

$$\phi \;=\; \phi_0 \;+\; n\,\frac{2\pi}{5} \tag{163}$$

where the integer n runs from 1 to 5. The trapped beam jumped from island to island, advancing two islands every turn of the accelerator, in a pattern that repeated every 5 turns. The trapped beam did not filament, and so delivered a coherent turn-by-turn "persistent" signal that was observed on two horizontal beam position monitors that were separated in phase by about 90°.

A typical set of raw persistent signal data, from one of the beam position monitors, is shown in Figure 9 for 64,000 turns, or about 1.4 seconds. Tune modulation was turned on at 9,000 turns, becoming visible as an amplitude modulation of the islands at about 28,000 turns. The persistent signal started dropping dramatically at about 32,000 turns, eventually driving all of the trapped beam out of the resonance island. This signal decay occurred due to a tune modulation chirp that was externally driven by iron-free quadrupoles. These quadrupoles were originally used in a tune feedback loop when the Tevatron operated in a slow extraction (fixed target) mode. The ripples that are clearly visible between 30,000 and 50,000 turns indicate the increasing frequency of the chirp.

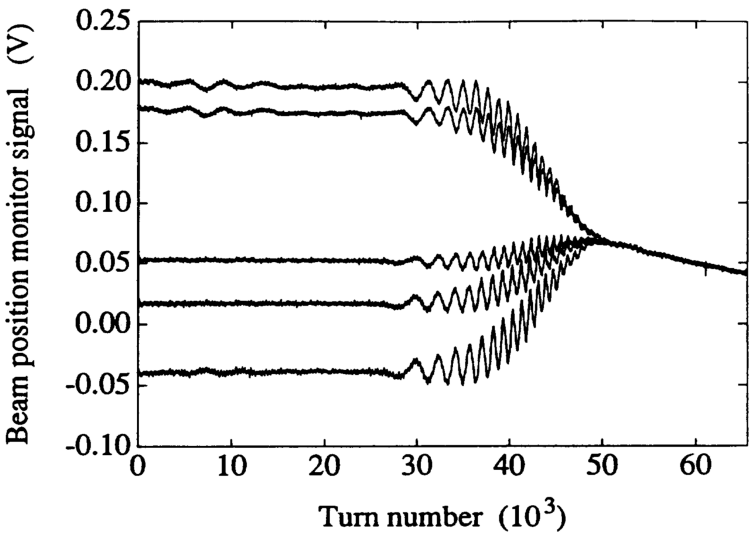


Figure 9: Raw digitized signals of a beam position monitor, showing a persistent signal and its response to a tune modulation chirp from $(q, Q_M) = (0, 0)$ to $(q, Q_M) = (0.0102, 0.0031)$. The nonzero average initial value is due to a closed orbit offset [27].

6.1 Data analysis and a summary of E778 results

The analysis of raw persistent signal data is illustrated in Figure 10 for a different data set, also with a tune modulation chirp, over about 5 seconds. Fourier analysis of the raw beam position monitor data showed a dominant peak at exactly $Q_x = 0.4$, with an amplitude that represented the size of the islands under the assumption that the island was evenly filled with protons. The amplitude of the $Q_x = 0.4$ peak shown in the waterfall plot on the left of Figure 10 is shown on the right as a function of time. The disappearance of the persistent signal amplitude at about 170,000 turns (3.6 seconds) indicates that the boundary between the amplitude modulation and chaos partitions was crossed at that time.

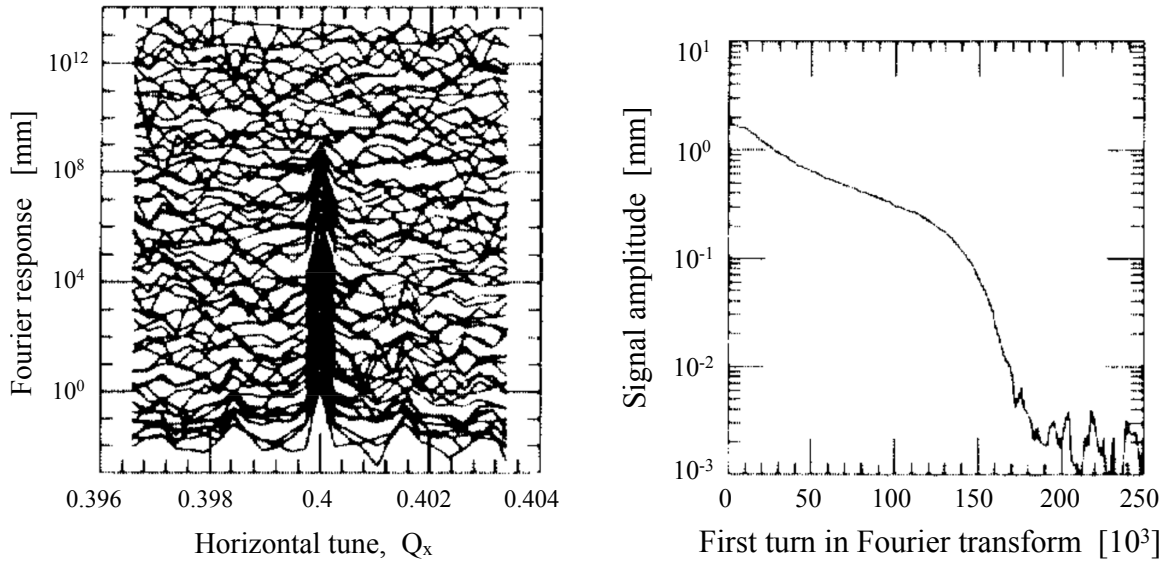


Figure 10: Analysis of the effect of a tune modulation chirp on raw persistent signal data in E778. Left: A waterfall plot of a sequence of Fourier analyses of a persistent signal, showing signal loss during the chirp [25]. Right: Evolution of the $Q_x = 2/5$ Fourier peak during the chirp.

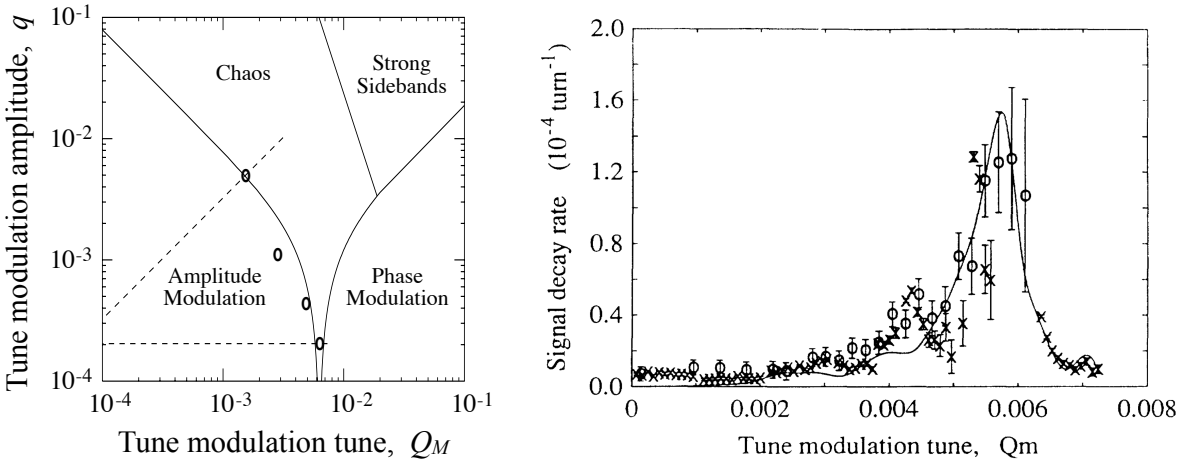


Figure 11: Determining that the island tune is $Q_I = 0.0063$ by locating the boundary between the amplitude modulation and chaos partitions in (q, Q_M) space [15, 27]. Left: Boundary measurements for each of four chirp trajectories, derived from the signal decay rates. Right: The decay rate of the persistent current signal as a function of the tune modulation tune Q_M, and multi-particle simulation results (solid line).

The universal model that predicts the partitions in (q, Q_M) space, shown in Figure 7, has only a single free parameter, the island tune Q_I. Thus, locating one or more of the partition boundaries enables Q_I to be inferred, in a best fit to the data. This is illustrated in Figure 11 for four data sets with different chirp trajectories, including the data set shown in Figure 10. The four oval symbols in the left sub-plot mark the locations at which the persistent signal was completely lost, for each of the chirp trajectories that pass through them. The four boundary markers are well fit by an island tune of $Q_I = 0.0063$. Unfortunately the other partition boundaries – at higher amplitudes and higher frequencies – were not readily accessible in the E778 experiment, limited by the inductance of the tune modulation quadrupoles.

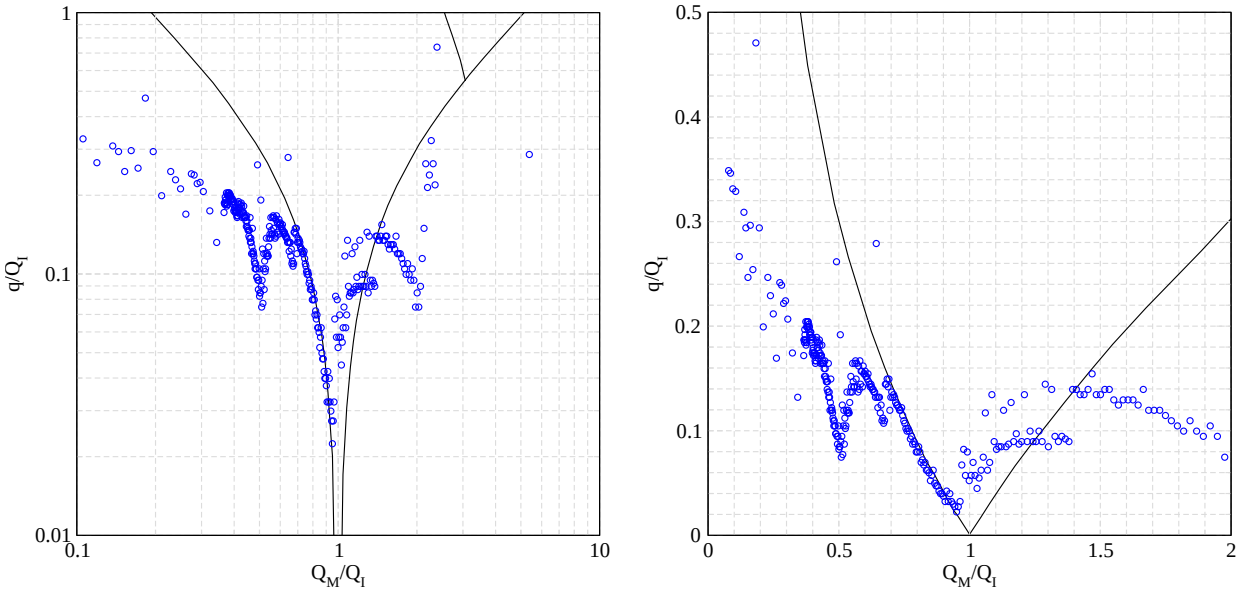


Figure 12: Locating the boundaries in (q, Q_M) space by simulation, with a known island tune $Q_I \approx 0.004$ and $N = 4$. The left and right plots are the same data; left is log-log axis scaling, right is linear-linear axis scaling. Each small blue circle represents a simulation at constant Q_M in which q is gradually increased until the fixed point is lost in a sea of chaos.

6.2 Fine structure in the partition boundaries

The solid line in the right sub-plot of Figure 11 represents simulation results obtained by tracking an evenly populated island, under the influence of identical experimental conditions and applying identical data reduction techniques. Both E778 data and such simulation results showed evidence of structure at modulation tunes Q_M below the island tune. It was speculated that these features were due to parametric modulation of the resonance strength, leading to Mathieu (parametric) resonances at a family of modulation tunes given by

$$Q_M \;=\; \frac{2Q_I}{n} \tag{164}$$

for any integer n [25, 26].

The single particle tracking results shown in Figure 12 support this speculation, using a very simple lattice with a linear phase advance and a single octupole to drive both detuning and an $N = 4$ resonance to first order. These results are similar to those previously published [15] from an octupole/decapole lattice with $N = 5$. Figure 12 confirms that there is additional structure to the (Q_M, q) parameter space boundaries. Each small blue circle represents a phase simulation at constant Q_M where q is gradually increased and the fixed point is "followed" until is submerged in a sea of chaos. Figure 13 shows four representative phase space plots of this modulated phase space for $Q_M/Q_I = 0.8$ and increasing values of q/Q_I.

This fine structure could be explored through further simulation studies, even in the absence of RHIC beam experiments. For example, this structure could be compared to the Mathieu equation stability diagram (see for example Figure 3 of [28]) in order to determine if further stability diagram refinements are warranted, and possible.

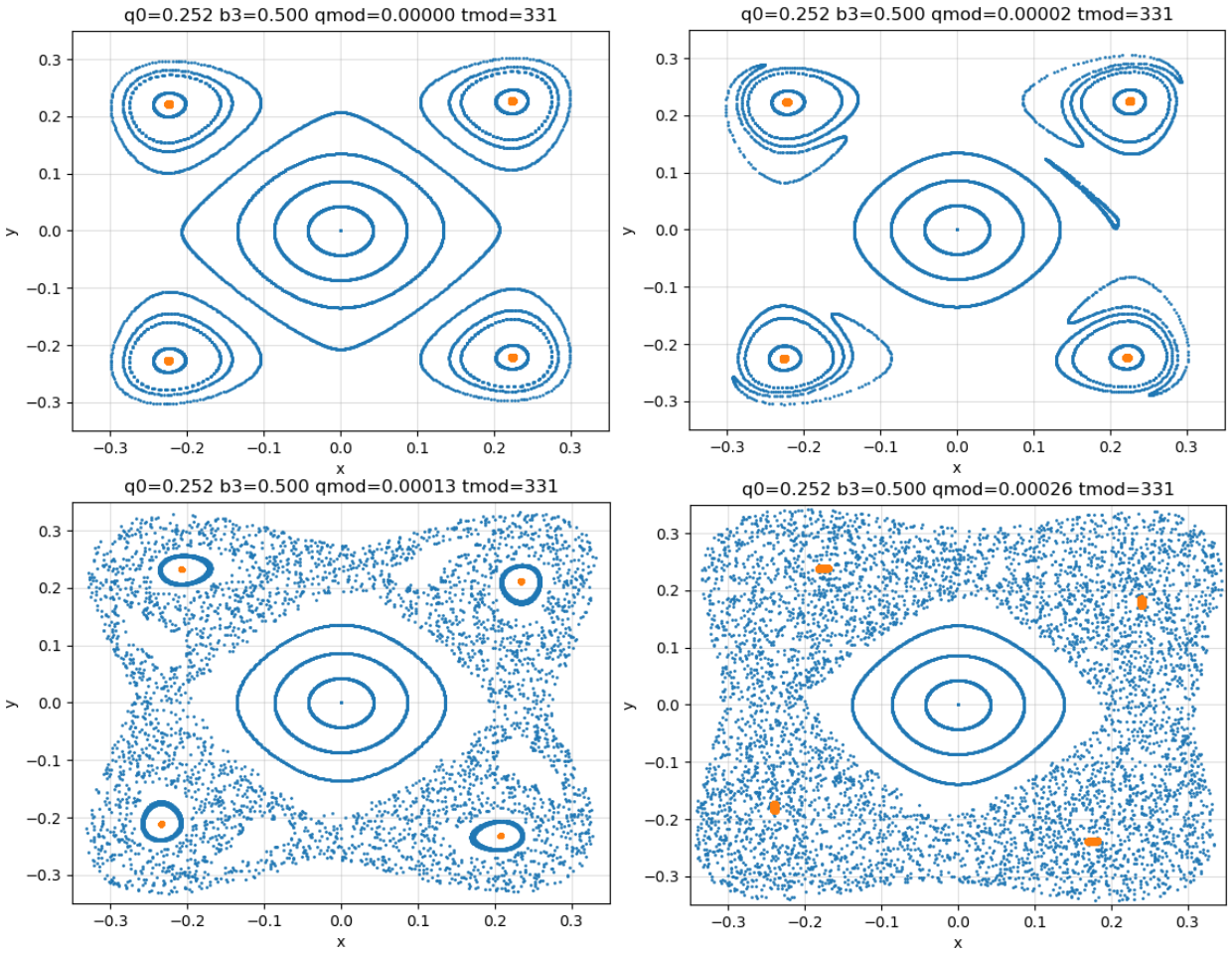


Figure 13: Representative phase space portraits from the simulation used to generate Figure 12, as q/Q_I increases along a line of constant $Q_M/Q_I = 0.8$. Fixed points are orange.
Top Left: $q/Q_I = 0$, unperturbed phase space.
Top Right: q/Q_I just above zero, showing barely perturbed phase space and additional resonance formation.
Bottom Left: $q/Q_I \approx 0.4$, showing the breakdown of separatrices and the formation of large scale chaos.
Bottom Right: $q/Q_I \approx 0.8$, with fixed points almost entirely subsumed by chaos.

7 Summary

Beam experiments in RHIC are necessary and possible, if the Resonance Island Jump scheme is to be considered seriously for the HSR.

The potential for RIJ-related beam experiments in RHIC. Small amplitude motion around the closed orbit is characterized by Twiss parameters, tune, chromaticity, and the transition gamma $(x_{CO}, x'_{CO}, \beta_x, \alpha_x, Q_x, \chi_x, \gamma_T)$. Beam trapped in one or N resonance islands is characterized by local and global parameters: $(x_I, x'_I, \beta_I, \alpha_I)$ and $(Q_I, \chi_I, \gamma_{TI})$. A successful RIJ scheme would exploit a large value of $|\gamma_T - \gamma_{TI}|$ by using a fast kicker to move beam quickly from closed orbit to island, or vice versa.

A successful RHIC experiment would measure and compare on-axis and island parameter differences, and compare them against theoretical predictions. Many octupoles would be powered to mimic an HSR implementation. A simple experiment would trap beam by adiabatically opening or closing islands, with or without an energy ramp. A more productive experiment would use a fast kicker. However, no appropriate kicker is currently available in RHIC. This technical note provides the theoretical underpinnings for such an experiment, but leaves unresolved the detailed planning.

Octupoles and detuning. The RHIC correction scheme includes 90 octupoles, each with a range of strengths $(K3.L)_{range} = \pm 45.02$ m^{-3} at injection energy, and ± 4.08 m^{-3} at storage. They are driven by 24 power supplies. The corresponding ranges of the detuning coefficients $(\kappa_{xx}, \kappa_{xy}, \kappa_{yy})$ are given in Table 3 for injection and storage lattices in both RHIC and HSR.

Motion close to the 1/4 resonance. Near-resonant horizontal motion is described by a Kobayashi Hamiltonian H_4 that, when differentiated, describes the small increment in action and phase accumulated over 4 turns. The key Hamiltonian coefficients $(\Delta Q, V_{40}, V_{44})$ parameterize the separation of base and resonance tunes, the rate of detuning with action, and the resonance driving strength, respectively. This description predicts the action of the fixed point, the resonance island width, and the island tune Q_I – a vital parameter that more fundamentally characterizes the resonance strength.

Evaluating the resonance driving vector $\bar{V}_{44}$. The length and direction of the resonance driving vector are vital in determining the action and phases of the fixed points at the center of the 4 resonance islands. Each octupole contributes a component vector to the sum vector, with a length proportional to its strength $(K3.L)$ and to β^2 at the octupole.

The vector sensitivity $\bar{S}_{44}$ of each power supply is found by summing over all the octupoles that it drives. The 12 sensitivities for power supplies driving F-octupoles are about an order of magnitude longer than the 12 D-octupole sensitivities. Six F-octupole power supplies dominate the situation, and enable the other 6 F-octupole and all 12 D-octupole power supplies to be ignored. Those 6 vectors point mostly in 3 directions that are separated by about 60 degrees, leading to their natural combination into 3 essentially orthogonal 'effective' power supplies.

Ramping and modulating the tune. Tune modulation with amplitude q at a tune Q_M is inherent in transverse motion (at the synchrotron tune Q_s, through non-zero chromaticity) and also enables a powerful experimental technique. Canonical transformations of the Kobayashi Hamiltonian help lead to the prediction that (q, Q_M) tune modulation parameter space is partitioned into four areas that display radically different behavior: amplitude modulation, phase modulation, strong sidebands, and chaos. There is only one free variable – Q_I, the island tune – because the partition boundaries are universal when plotted in $(q/Q_I, Q_M/Q_I)$ space. The island tune Q_I can be measured by observing the loss of the persistent signal generated by beam trapped in a resonance island, when an externally controlled tune modulation is chirped across a partition boundary. The RHIC transition jump quadrupoles can be re-purposed to modulate the tune.

Tune modulation and data reduction techniques. The dynamics of a metastable beam of particles trapped in artificially excited resonance islands were studied in the Tevatron in the late 1980's and early 1990's, as part of the Fermilab E778 nonlinear beam dynamics experiment. Persistent signals disappeared when the tune modulation parameters crossed a partition boundary.

Simulations with octupoles and tune modulation confirm the general location of the partition boundaries, but also show fine structure of what appear to be a family of Mathieu resonances, particularly near the boundary between "amplitude modulation" and "chaos". This fine structure could be explored through further simulation studies, even in the absence of RHIC beam experiments.

Appendices

A Key equations

The physical and normalized strengths of a single thin octupole (see Equation 20) are

$$\begin{aligned} g_p\,[\mathrm{m}^{-3}] &= \frac{L}{6}\frac{1}{(B\rho)}\frac{d^3B_y}{dx^3} = \frac{1}{6}K3.L \\ g\,[\mathrm{m}^{-1}] &= \frac{\beta^2}{6}K3.L \end{aligned} \tag{165}$$

The three independent detuning coefficients (see Equation 38) are

$$\begin{aligned} \kappa_{xx} &= \frac{1}{16\pi}\sum_{\text{supplies}} K3.L\left(\sum_{\text{octupoles}}\beta_x^2\right) \\ \kappa_{xy} &= \frac{-1}{8\pi}\sum_{\text{supplies}} K3.L\left(\sum_{\text{octupoles}}\beta_x\beta_y\right) \\ \kappa_{yy} &= \frac{1}{16\pi}\sum_{\text{supplies}} K3.L\left(\sum_{\text{octupoles}}\beta_y^2\right) \end{aligned} \tag{166}$$

The detuning term (see Equation 74) is

$$V_{40} = \pi\kappa = \frac{1}{16}\sum_{\text{supplies}} K3.L\left(\sum_{\text{octupoles}}\beta^2\right) \tag{167}$$

The resonance Hamiltonian representing four-turn motion close to the resonance (see Equation 81) is

$$H_R(I,\psi) = V_{40}\,I^2 + V_{44}J_{FP}^2\cos(4\psi) \tag{168}$$

The island half width (see Equation 88) is

$$I_{HW} = \pi\left|\frac{2V_{44}}{V_{40}^3}\right|^{1/2}|\Delta Q| \tag{169}$$

The island tune (see Equation 101) is

$$Q_I = \frac{1}{\pi}\left(8\,V_{40}.V_{44}\right)^{1/2}\cdot J_{FP} \tag{170}$$

Alternatively, the island tune (see Equation 102) can be written

$$Q_I = \left|\frac{8\,V_{44}}{V_{40}}\right|^{1/2}\cdot|\Delta Q| \tag{171}$$

The change in action over four turns (see Equation 105) is

$$\Delta J = -16\,V_{44}\,J^2\cos(4\psi+\psi_{444}) \tag{172}$$

The resonance driving vector (see Equation 120) is

$$\vec{V}_{44} \equiv V_{44}\begin{pmatrix}\sin(\psi_{444})\\ \cos(\psi_{444})\end{pmatrix} = -\frac{1}{48}\sum_{\text{supplies}} K3.L\left(\sum_{\text{octupoles}}\beta^2\begin{pmatrix}\sin(4\theta-\pi/2)\\ \cos(4\theta-\pi/2)\end{pmatrix}\right) \tag{173}$$

The resonance driving vector is given in terms of the sensitivity vectors (see Equation 121) by

$$\vec{V}_{44} = \sum_{\text{supplies}}(K3.L)\,\vec{S}_{PS} \tag{174}$$

B Phase spaces, action-angle co-ordinates, emittance, and beam size

The Floquet matrix

$$T \;=\; \begin{pmatrix} 1/\sqrt{\beta} & 0 \\ \alpha/\sqrt{\beta} & \sqrt{\beta} \end{pmatrix} \tag{175}$$

and its inverse

$$T^{-1} \;=\; \begin{pmatrix} \sqrt{\beta} & 0 \\ -\alpha/\sqrt{\beta} & 1/\sqrt{\beta} \end{pmatrix} \tag{176}$$

depend on the periodic Twiss parameters β and α at the observation point in a storage ring. They transform physical phase space co-ordinates into normalized phase space co-ordinates (with tildes) through

$$\begin{pmatrix} \tilde{x} \\ \tilde{x'} \end{pmatrix} \;=\; T \begin{pmatrix} x \\ x' \end{pmatrix} \tag{177}$$

and vice versa

$$\begin{pmatrix} x \\ x' \end{pmatrix} \;=\; T^{-1} \begin{pmatrix} \tilde{x} \\ \tilde{x}' \end{pmatrix} \tag{178}$$

in the horizontal plane. While x has the dimension of length, and x' is dimensionless, both $\tilde{x}$ and $\tilde{x}'$ have the dimension of root length.

Normalized co-ordinates $(\tilde{x}, \tilde{x}')$ are related to normalized amplitude and phase $(\tilde{a}, \phi)$ through

$$\begin{pmatrix} \tilde{x} \\ \tilde{x}' \end{pmatrix} \;=\; \tilde{a} \begin{pmatrix} \sin(\phi) \\ \cos(\phi) \end{pmatrix} \tag{179}$$

showing that the normalized amplitude is simply

$$\tilde{a} \;=\; \sqrt{\tilde{x}^2 + \tilde{x}'^2} \tag{180}$$

Linear motion in normalized phase space describes a circle. All three normalized parameters $\tilde{a}, \tilde{x}$ and $\tilde{x}'$ have the dimensions of root length.

Using action-angle co-ordinates (J, ϕ) this becomes

$$\begin{pmatrix} \tilde{x} \\ \tilde{x}' \end{pmatrix} \;=\; \sqrt{2J} \begin{pmatrix} \sin(\phi) \\ \cos(\phi) \end{pmatrix} \tag{181}$$

showing that

$$\tilde{a} \;=\; \sqrt{2J} \tag{182}$$

Action J, with the dimension of length, is usually quantified in meters or – like emittance – in microns.

Physical co-ordinates (x, x') connect to action-angle co-ordinates (J, ϕ) through

$$\begin{pmatrix} x \\ x' \end{pmatrix} \;=\; \sqrt{2J} \begin{pmatrix} \sqrt{\beta}\sin(\phi) \\ -(\alpha/\sqrt{\beta})\sin(\phi) + (1/\sqrt{\beta})\cos(\phi) \end{pmatrix} \tag{183}$$

showing that the physical displacement x oscillates with an amplitude

$$a \;=\; \sqrt{2J\beta} \tag{184}$$

that depends on the Twiss parameter β at the observation point. Both a and β have the dimension of length. Plotting (x, x') over the continuous range of potential horizontal betatron phases

$$-\infty \;<\; \phi \;<\; \infty \tag{185}$$

with constant J traces out the phase space ellipse described by Equation 183 and drawn in Figure 14. The ellipse has an area

$$A \;=\; 2\pi J \tag{186}$$

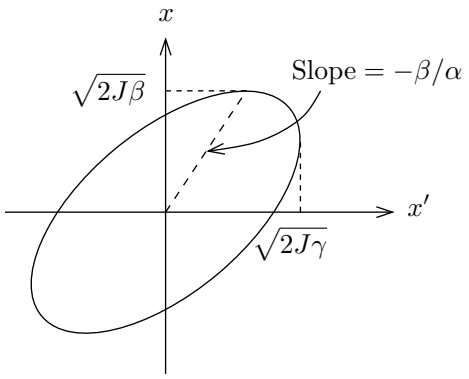


Figure 14: The physical phase space ellipse with action J at a location with Twiss parameters (β, α, γ).

The equivalent circle in normalized phase has the same area A.

Action is calculated from the physical co-ordinates observed on turn n by

$$2J_n \;=\; \beta\, x_n'^2 \;+\; 2\alpha\, x_n x_n' \;+\; \gamma\, x_n^2 \tag{187}$$

Linear motion observed once per turn is especially simple in action-angle space (J, ϕ), since

$$\begin{aligned} J_n &= J \;=\; \text{constant} \\ \phi_n &= 2\pi Q.n \;+\; \phi_0 \end{aligned} \tag{188}$$

where Q is the horizontal tune.

B.0.1 Unnormalized emittance, average action, and beam size

The RMS horizontal displacement of a single particle, observed over many turns at the observation point, is

$$\begin{aligned} \sigma_1 &\equiv \left\langle x^2 \right\rangle^{1/2} \;=\; 2\sqrt{J\beta}\left\langle \sin^2(\phi_n) \right\rangle^{1/2} \\ &= \sqrt{J\beta} \end{aligned} \tag{189}$$

Thus, the mean square horizontal size of a bunch of particles with an action distribution $\rho(J)$ is

$$\begin{aligned} \sigma^2 &= \frac{1}{M}\int_0^\infty \sigma_1^2\, \rho(J)\, dJ \;=\; \frac{\beta}{M}\int_0^\infty J\, \rho(J)\, dJ \\ &= \beta\, \langle J \rangle \end{aligned} \tag{190}$$

where the bunch population is

$$M \;=\; \int_0^\infty \rho(J)\, dJ \tag{191}$$

On the other hand the mean square size can also be written

$$\sigma^2 \;=\; \beta\, \epsilon_u \tag{192}$$

where ϵ_u is the unnormalized horizontal RMS emittance. Comparing Equations 189 and 192 gives

$$\epsilon_u \;=\; \langle J \rangle \tag{193}$$

and shows that the unnormalized emittance is simply the average action of a bunch.

C Fixed point finder

Motion around a non-trivial (non-zero) fixed point (x_c, y_c) of a 2-dimensional N-turn map can be closely modeled by the concatenation of three linear transformations:

- translation by $(-x_c, -y_c)$
- rotation by a 2D rotation matrix $R \equiv \begin{pmatrix} C & S \\ -S & C \end{pmatrix}$, where $C \equiv \cos(2\pi Q_I N)$, $S \equiv \sin(2\pi Q_I N)$
- translation by (x_c, y_c)

This model improves as one moves closer to the fixed point and motion approximates that of a simple harmonic oscillator with island tune Q_I. Note that this transformation transforms the fixed point to itself.

This transformation operating on a fixed point guess (x_0, y_0) to produce (x_0', y_0') can be written in matrix terms as

$$\begin{aligned} \begin{pmatrix} x_0' \\ y_0' \end{pmatrix} &= R \begin{pmatrix} x_0 - x_c \\ y_0 - y_c \end{pmatrix} + \begin{pmatrix} x_c \\ y_c \end{pmatrix} \\ &= \begin{pmatrix} Cx_0 - Cx_c + Sy_0 - Sy_c + x_c \\ -Sx_0 + Sx_c + Cy_0 - Cy_c + y_c \end{pmatrix} \end{aligned} \tag{194}$$

Also consider the motion of two perturbed initial points $(x_0 + \delta, y_0) \to (x_1', y_1')$ and $(x_0, y_0 + \delta) \to (x_2', y_2')$ under this transformation:

$$\begin{pmatrix} x_1' \\ y_1' \end{pmatrix} = \begin{pmatrix} Cx_0 + C\delta - Cx_c + Sy_0 - Sy_c + x_c \\ -Sx_0 - S\delta + Sx_c + Cy_0 - Cy_c + y_c \end{pmatrix} \tag{195}$$

$$\begin{pmatrix} x_2' \\ y_2' \end{pmatrix} = \begin{pmatrix} Cx_0 + -Cx_c + Sy_0 + S\delta - Sy_c + x_c \\ -Sx_0 + Sx_c + Cy_0 + C\delta - Cy_c + y_c \end{pmatrix} \tag{196}$$

Subtracting Equation 194 from Equations 195 and 196 gives:

$$\begin{pmatrix} x_1' - x_0' \\ y_1' - y_0' \\ x_2' - x_0' \\ y_2' - y_0' \end{pmatrix} = \begin{pmatrix} C\delta \\ -S\delta \\ S\delta \\ C\delta \end{pmatrix} \tag{197}$$

These results can be used to calculate average values of C and S (and thus Q_I) from simulated map iterations. This converges best when δ is very small compared to the island width.

Though one perturbation is strictly all that is needed for C and S calculations, the orthogonal perturbations ensure that at least one rotation is not parallel transport, and thus not degenerate.

To find the estimate of the fixed point (x_c, y_c) for this iteration, one can decompose Equation 194 into the linear terms in (x_c, y_c) and a homogeneous term:

$$\begin{pmatrix} x_0' \\ y_0' \\ 1 \end{pmatrix} = \begin{pmatrix} 1 - C & -S & Cx_0 + Sy_0 \\ S & 1 - C & -Sx_0 + Cy_0 \\ 0 & 0 & 1 \end{pmatrix} \begin{pmatrix} x_c \\ y_c \\ 1 \end{pmatrix} \tag{198}$$

Inverting this 3x3 matrix gives a next guess for the fixed point (x_c, y_c). The next iteration should use a value of δ that is substantially smaller than the distance from the previous fixed point guess (x_0, y_0) and the new fixed point guess (x_c, y_c); sufficient smallness of this iterated δ can also be used as a convergence criterion.

References

[1] M. Giovannozzi et al. 2021. A novel non-adiabatic approach to transition crossing in a circular hadron accelerator. *Eur. Phys. J. Plus (2021) 136:1189.*

[2] S. Wang. 2023. Using non-linear beam dynamics to mitigate disturbances during acceleration in circular accelerators. *MSci thesis, Imperial College, London & EPFL, Lausanne.*

[3] S. Peggs, A. Drees, H. Lovelace III, G. Robert-Demolaize. 2023. HSR transition jump optics in the September 2022 layout. *BNL EIC technical note.* EIC-ADD-TN-41.

[4] M. Giovanozzi et al. 2006. The CERN PS multi-turn extraction based on beam splitting in stable islands of transverse phase space: Design Report. *CERN-2006-011.*

[5] S. Gilardoni at el. 2006. Experimental evidence of adiabatic splitting of charged particle beams using stable islands of transverse phase space. *Physical Review Special Topics - Accelerators and Beams.* PRST-AB 9, 104001 (2006).

[6] A. Franchi et al. 2009. *Phys. Rev. ST Accel. Beams 12, 014001.*

[7] E. Benedetto et al. 2010. Results from the 2009 Beam Commissioning of the CERN Multi-turn Extraction *IPAC 10, p. 3619 (2010).*

[8] A. Bazzani et al. 2014. *Phys. Rev. E 89, 042915.*

[9] J. Borburgh et al. 2016. *EPL 113 34001 (2016).*

[10] S. Peggs, R. Talman. 1986. Empirical Hamiltonians. *SSC technical note; High Energy Accelerator Conference.* SSC-84; HEACC-86-566.

[11] RHIC Configuration Manual. 2006. Table 11-4, p. 25.

[12] Table 7-3, page 59. 2006. RHIC Configuration Manual. *BNL EIC technical note.* EIC-ADD-TN-56.

[13] T. Tutone. 1981. *867-5309/Jenny.* https://www.youtube.com/watch?v=6WTdTwcmxyo .

[14] S. Peggs. 1988. Hamiltonian Theory of the E778 Nonlinear Dynamics Experiment. *SSC technical note; CERN technical note; ICFA Lugano workshop.* SSC-175; CERN 88-04.

[15] T. Satogata. 1993. Nonlinear Resonance Islands and Modulational Effects in a Proton Synchrotron. *Northwestern University.* Ph.D. thesis.

[16] Y. Kobayashi. 1970. Theory of the resonant beam ejection from synchrotrons. *Nuclear Instruments and Methods* **83** *77-80* .

[17] H. Goldstein. 2002. Classical Mechanics, Chapter 9. *Addison-Wesley.*

[18] S. Peggs, T. Satogata. 2017. Introduction to Accelerator Dynamics. *Cambridge University Press.* DOI: 10.1017/9781316459300.

[19] L. Merminga et al. 1988. An experimental study of the SSC magnet aperture criterion. *EPAC 1988, p. 791.*

[20] A. Chao et al. 1988. Experimental investigation of nonlinear dynamics in the Fermilab Tevatron. *Physical Review Letters, Volume 61, Number 24.*

[21] A. Chao et al. 1988. A progress report on Fermilab experiment E778. *SSC technical note; Fermilab technical note.* SSC-156; FN-471.

[22] L. Merminga et al. 1989. Nonlinear dynamics experiment in the Tevatron. *PAC 1989, p. 1429.*

[23] T. Chen, S. Peggs. 1989. The driven pendulum, and E778 tune modulation. *PAC 1989, p. 1343.*

[24] S. Peggs. 1989. Nonlinear dynamics ion the SSC: experiment E778. *SSC technical note; Advanced Study Institute on Techniques and Concepts of High Energy Physics, St. Croix.* SSC-216.

[25] G. Tsironis, S. Peggs, T. Chen. 1990. Tune modulation, Mathieu stability, and the driven pendulum. *EPAC 1990, p. 1753.*

[26] T. Satogata, S. Peggs. 1991. Is beta modulation more or less potent than tune modulation? *PAC 1991, p. 476.*

[27] T. Satogata et al. 1992. Driven Response of a Trapped Particle Beam. *Physical Review Letters, Volume 68, Number 12.*

[28] I. Kovacic et al. 2018. Mathieu's Equation and Its Generalizations: Overview of Stability Charts and Their Features. *Appl. Mech. Rev.* **70** 020802-1, March 2018, `http://audiophile.tam.cornell.edu/randpdf/AMR.pdf`.